Open access • Journal Article • DOI:10.1007/BF00032340

Part-circular surface cracks in round bars under tension, bending and twisting

— Source link

A. Levan, Jean-Jacques Royer

Institutions: École centrale de Nantes

Published on: 01 May 1993 - International Journal of Fracture (Kluwer Academic Publishers)

Topics: Crack closure, Stress intensity factor, Fracture mechanics and Bending moment

Part-circular surface cracks in round bars under tension, bending and twisting

Anh Le Van, Jean Royer

Part-circular surface cracks in round bars under tension, bending and twisting

A. LEVAN and J. ROYER
Laboratoire de Mécanique des Structures, Ecole Centrale de Nantes, 1 rue de la Noë, Nantes 44072 Cedex 03, France

Abstract. Circular-fronted cracks in round bars subject to tension, bending and twisting are considered. Numerical expressions are given allowing the calculation of stress intensity factors K_I, K_{II}, K_{III} at every point on the crack front for a wide range of crack geometries. Comparisons are made with analytical, experimental and numerical results available in the literature. Crack shapes satisfying the iso-K_I criterion are also determined, making it possible to investigate the problem of crack growth behaviour under tensile or bending fatigue loads.

1. Introduction

As cylindrical specimens are easily machined, components with a round cross section are commonly used in engineering structures. Bars, shafts, wires, reinforcements, bolts, screws or pins are examples of cylindrically-shaped structural elements. In many applications the loading conditions are quite complex. Under cyclic or repeated loads, fatigue cracks can occur in such components. Experimental works [1–5] showed that surface cracks created by fatigue have approximately circular fronts. In order to predict the growth of such a crack and the strength of the cracked component, an accurate stress analysis is required. Under linear elastic conditions, this leads us to precisely calculate the stress intensity factors which govern the mechanical state in the structure. In the general case of a combined load, a mixed mode I + II + III situation exists along the crack front. As in any arbitrary three-dimensional configuration, the variation of stress intensity factors K_I, K_{II}, K_{III} on the crack front must be taken into account.

Several works have been devoted to the problem of a surface crack in a round bar. Table 1 summarizes the main features of some studies relating to this problem. In Table 1, K_{IA} denotes the stress intensity factor at the deepest point of the crack, K_{IB} the stress intensity factor at the surface terminal point (intersection between the lateral surface and the crack front), $\bar{K}_I$ the average stress intensity factor calculated on the crack front. Additionally, straight-fronted cracks are considered as particular cases of circular or semi-elliptical cracks. The bibliography, although representative, makes no claim to completeness – rather, it is a selection of the many references found in this field.

In this paper, use is made of a boundary integral equation specifically developed for fracture problems [22] to determine the stress intensity factors K_I, K_{II}, K_{III} for circular-fronted cracks in a round bar subjected to tension, bending and torsion. Polynomial expressions are provided allowing the calculation of these stress intensity factors at every point on the crack front for a wide range of crack geometries. Crack shapes satisfying the iso-K_I criterion are computed, and the problem of crack growth behaviour under tensile or bending fatigue loads is discussed. The results are compared with other experimental and numerical results available in the literature

Table 1. Summary review

Reference	Crack geometry	Load	Method	Main results
Experimental works				
Bush (1976) [6]	Straight-fronted crack	Three-point bending	Compliance measurements	$\bar{K}_I$
Daoud et al. (1978) [7]	Straight-fronted crack	Tension	Compliance measurements	$\bar{K}_I$
Astiz et al. (1981) [8]	Straight-fronted crack	Tension	Photoelasticity	K_{IA}
Salah el din et al. (1981) [2]	Actual shape ≈ circular frontal crack	Tension and bending	Fatigue tests	K_{IA}
Bush (1981) [9]	Straight-fronted crack	Tension	Compliance measurements	$\bar{K}_I$
Athanassiadis et al. (1981) [1]	Actual shape ≈ circular fronted or semi-elliptical crack	Tension	Compliance measurements + Fatigue tests	$\bar{K}_I$ and the fracture toughness K_{IC}
Wilhem et al. (1982) [4]	Actual shape ≈ circular fronted crack	Tension	Fatigue tests	$\bar{K}_I$
Nezu et al. (1982) [3]	Actual shape ≈ circular fronted crack	Tension	Fatigue tests	A power law between crack propagation rate da/dN and range of stress intensity factor ΔK
Forman et al. (1986) [5]	Actual shape ≈ circular fronted crack + 90° intersecting angle	Tension and bending	Fatigue tests	$\bar{K}_I$
Astiz et al. (1986) [10]	Actual shape ≈ semi-elliptical crack	Tension	Fracture tests	K_{IA} at fracture

Reference	Crack geometry	Load	Method	Main results
Numerical works				
Blackburn (1976) [11]	Straight-fronted crack	Tension and bending	Finite element method (FEM)	$\bar{K}_I$
Daoud et al. (1978) [7]	Straight-fronted crack	Tension	2D-FEM and strain energy release rate computation	$\bar{K}_I$
Astiz et al. (1980) [12]	Straight-fronted crack	Tension	Stiffness derivative method	$\bar{K}_I$
Salah et din et al. (1981) [2]	Circular fronted crack	Tension and bending	FEM K_I by the displacement substitution method	K_{IA} and $\bar{K}_I$

Athanassiadis et al. (1981) [1]	Semi-elliptical crack	Tension, bending and compressive lateral bending	Boundary integral equation method	K_I at various locations on the crack front and $\bar{K}_I$
Nezu et al. (1982) [3]	Circular fronted crack	Tension	FEM	K_{IA} and K_{IB}
Fan et al. (1982) [13]	Circular fronted crack	Tension	Alternative method by coupling two analytical solutions to analogous problems	K_I along the crack front
Daoud et al. (1984) [14]	Straight-fronted crack	Bending	2D-FEM and strain energy release rate computation	$\bar{K}_I$
Daoud et al. (1985) [15]	Circular fronted crack One special crack shape	Tension and bending	2D-FEM and strain energy release rate computation	$\bar{K}_I$
Raju et al. (1986) [16]	Special crack geometries (≈ semi-elliptical) + 90° intersecting angle	Tension and bending	FEM K_I by the nodal force method	K_I along the crack front
Nord et al. (1986) [17]	Semi-elliptical crack	Tension and bending	FEM K_I by the stiffness derivative method	K_{IA} and K_{IB}
Astiz et al. (1986) [10], [18]	Semi-elliptical crack	Tension	FEM with incompatible singular element	K_I along the crack front
Caspers et al. (1987) [19]	Circular fronted crack	Tension and LATERAL bending	FEM and the weight function method	K_{IA} and K_{IB}

Other works

Reference	Crack geometry	Load	Method	Main results
Underwood et al. (1989) [20]	Straight-fronted crack	Three-point bending	Combination of: • experimental results of Bush [6] • numerical results of Daoud et al. [14] • two semi-analytical limit solutions	Two fitting K_I expressions for two span-diameter ratios
Si (1990) [21]	Circular fronted and semi-elliptical cracks	Tension and bending	Comparison of different works	Proposition of a K_I-factor solution verifying a hypothesis on the crack growth behaviour

for mode I crack problems. Comparisons are also made with analytical results for some limit configurations.

2. Formulation

2.1. Geometry

Figure 1 represents a round bar of radius R and height $h \gg R$ containing in its median cross section a surface crack. The crack front is part of a circle of radius R'. When R' equals the crack depth a, the crack is a so-called semi-circular crack. On the other hand, when R' tends to infinity, the crack is referred to as 'straight-fronted'. Any intermediate crack geometry between the two above limiting cases can be defined by the crack shape parameter $\alpha \equiv B_0B/B_0B_1$, $\alpha \in [0, 1]$ (Fig. 2). The computation is carried out on 4 crack shapes: $\alpha = 0$ (semi-circular), $\frac{1}{3}$, $\frac{2}{3}$ and 1 (straight-fronted). The two intermediate cracks have been determined in such a way that they divide arc B_0N_1 into three equal sub-arcs. Six relative crack depths are considered: $a/R = 0.04$, 0.12, 0.24, 0.40, 0.60, 0.85. Since there are 4 crack shapes for each crack depth, 24 crack geometries are analyzed (Fig. 3).

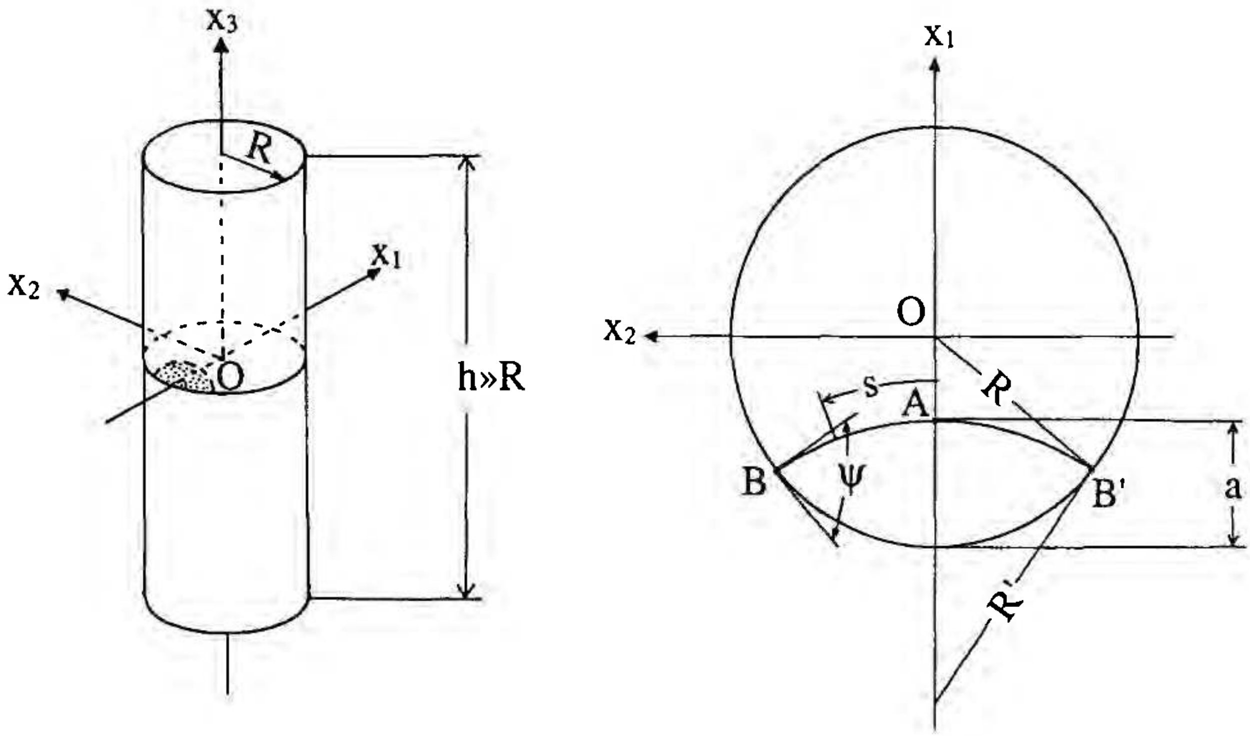

Fig. 1. Geometry.

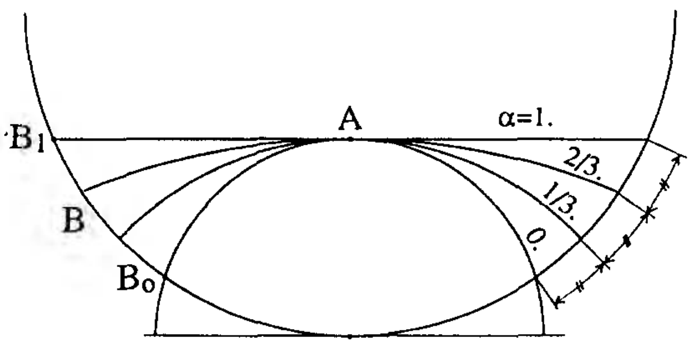

Fig. 2. Crack shapes defined by parameter α.

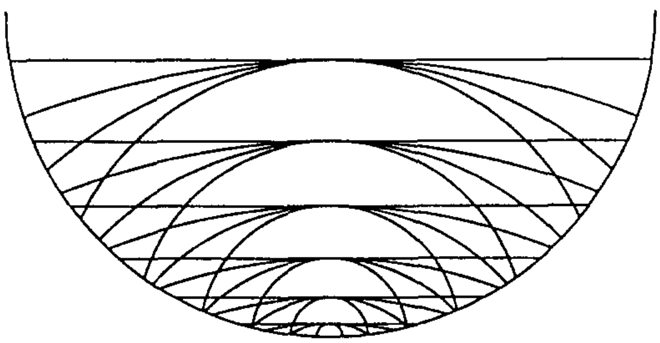

Fig. 3. Computed crack geometries.

2.2. *Loads*

The bar is successively subjected at its ends to three loads (Fig. 4):

- a uniform tensile stress σ.
- a linear tensile stress with outer fiber maximal value σ_m.
- a linearly distributed shear with outer fiber maximal value τ_m, resulting from torques twisting the bar.

As far as stress intensity factor solutions are concerned, these loads are respectively equivalent to a uniform pressure, a linear pressure and an axisymmetrical linear shear applied on the crack faces.

2.3. *Equations of the problem*

The bar is assumed to be made up of a homogeneous, isotropic, linear elastic material characterized by Young's modulus E and Poisson's ratio ν. For solving the problem use is made of the integral equation given in [22]. Let us introduce the following notations:

- x: field point with co-ordinates (x_1, x_2, x_3) in a rectilinear rectangular system of axes $O\mathbf{e}_1\mathbf{e}_2\mathbf{e}_3$ (Fig. 1)
- x_0: source point, $r = \|x - x_0\|$, $\mathbf{e}_r = (x - x_0)/r$ (Fig. 5)

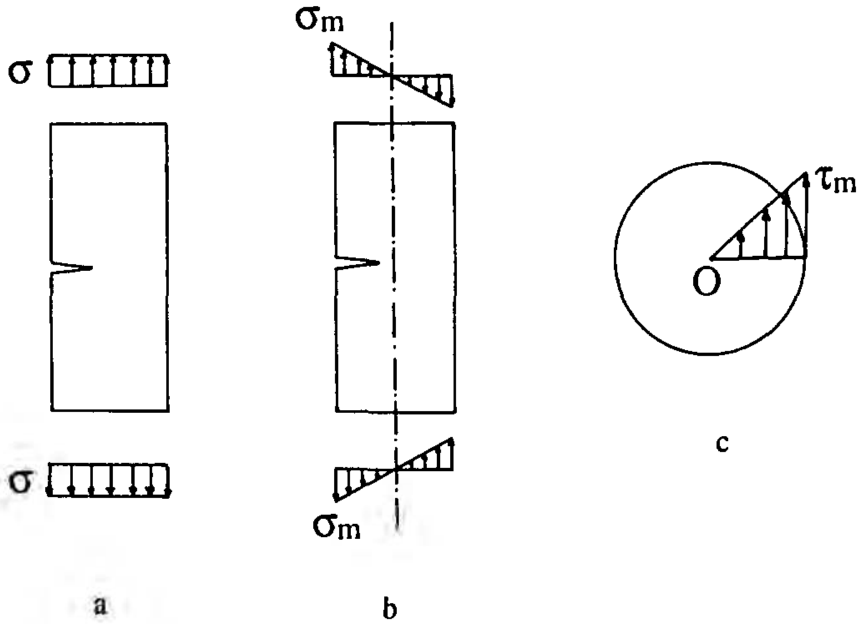

Fig. 4. Loads. (a) Tension. (b) Bending. (c) Torison.

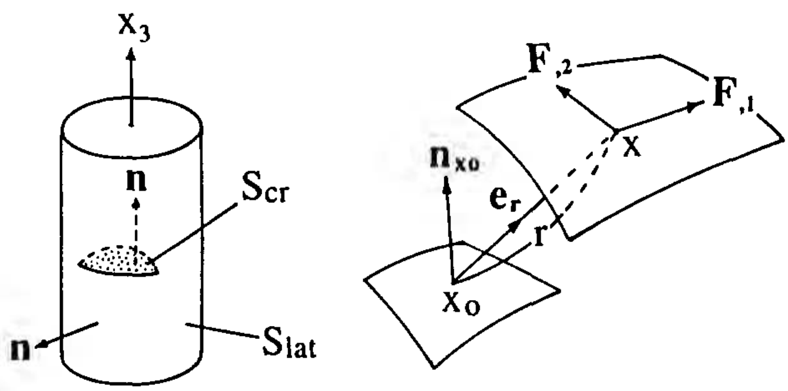

Fig. 5. Variables of the integral equation set.

- $\mathbf{t}(x_0, \mathbf{n}_{x0})$: the stress vector at x_0, related to normal $\mathbf{n}_{x0}$.
- S_{cr}: the surface of the crack, which is represented by a Cartesian parametrization

$$F_{cr}: \Delta_{cr} \ni (x_1, x_2) \to x \in S_{cr},$$

- S_{lat}: the cylindrical lateral surface of the bar, which admits the parameterization

$$F_{lat}: \Delta_{lat} = [0, 2\pi[\times [-h, h] \ni (\theta, x_3) \to x \in S_{lat}.$$

In fact, the lateral surface S_{lat} also includes the upper and lower flat bases of the bar, and another surface must be added at the junction of the bases and the cylindrical surface (Fig. 6) in order to avoid any discontinuity of the normal vector on S_{lat}. The outer surface of the bar is then sufficiently smooth as required by the theory.

- $\varphi_{cr}: S_{cr} \ni x \to \varphi_{cr}(x) \in \mathbb{R}^3$, $\varphi_{lat}: S_{lat} \ni x \to \varphi_{lat}(x) \in \mathbb{R}^3$: the unknown densities defined respectively on S_{cr} and S_{lat}, which are shown to be equal to the displacement jumps through the surfaces S_{cr} and S_{lat} respectively [23], [24].
- $\Phi_{cr} = \varphi_{cr} \circ F_{cr}$, $\Phi_{lat} = \varphi_{lat} \circ F_{lat}$ (compounds of functions F and φ).

The set of equations of the problem can then be written in the following form, which expresses the stress vector at any point x_0 and related to normal $\mathbf{n}_{x0}$, in terms of the densities φ_{cr} and φ_{lat}:

$$\begin{aligned} &\forall x_0 \in S_{cr}, \quad pv \int_{\Delta_{cr}} \mathrm{Ker}_{cr}(\phi_{cr}, x_0, x) \mathrm{d}x_1 \, \mathrm{d}x_2 + \int_{\Delta_{lat}} \mathrm{Ker}_{lat}(\phi_{lat}, x_0, x) \, \mathrm{d}\theta \, \mathrm{d}x_3 = \mathbf{t}(x_0, \mathbf{n}_{x0}), \\ &\forall x_0 \in S_{lat}, \quad \int_{\Delta_{cr}} \mathrm{Ker}_{cr}(\phi_{cr}, x_0, x) \mathrm{d}x_1 \, dx_2 + pv \int_{\Delta_{lat}} \mathrm{Ker}_{lat}(\phi_{lat}, x_0, x) \, \mathrm{d}\theta \, \mathrm{d}x_3 = \mathbf{t}(x_0, \mathbf{n}_{x0}), \end{aligned} \tag{1}$$

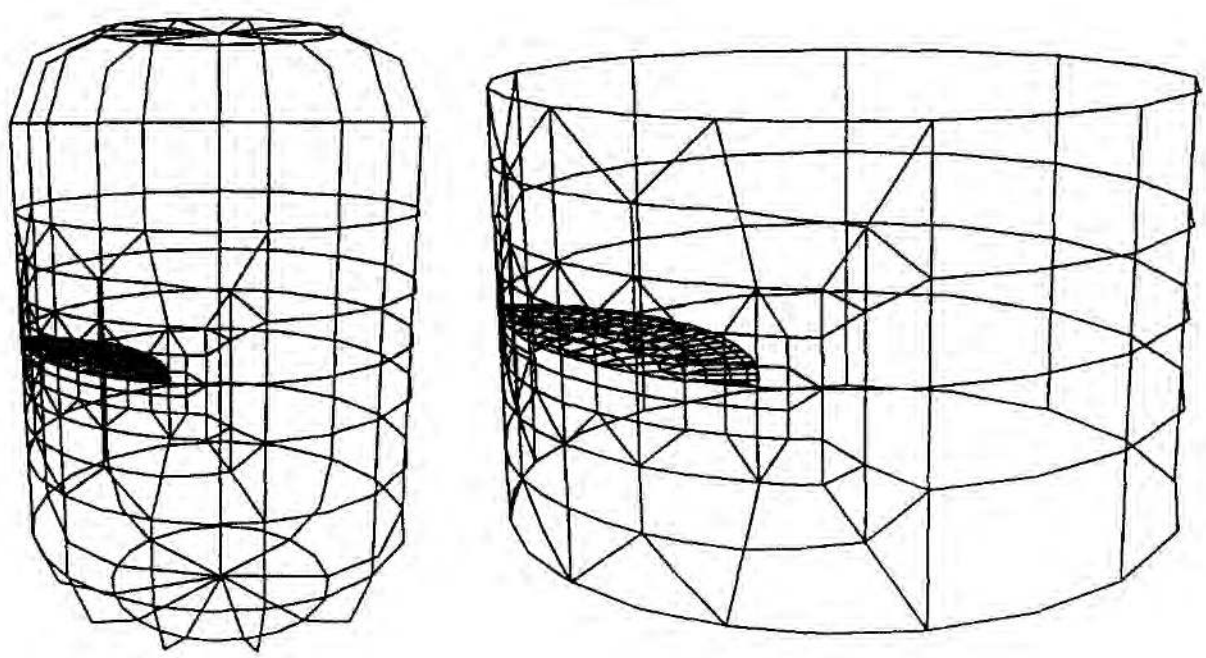

Fig. 6. Typical mesh modelling the cracked bar.

where $\mathrm{Ker_{cr}}$ and $\mathrm{Ker_{lat}}$ are the kernels defined by

$$\mathrm{Ker}(\Phi, x_0, x) = \frac{E}{16\pi(1-\nu^2)} \frac{\varepsilon_{3\alpha\beta}}{r^2} \{2(\mathbf{F}_{,\beta}, \Phi_{,\alpha}, \mathbf{e}_r)\mathbf{n}_{x0} - (1-2\nu)[(\Phi_{,\alpha}, \mathbf{e}_r, \mathbf{n}_{x0})\mathbf{F}_{,\beta}$$

$$+ (\mathbf{F}_{,\beta}\mathbf{n}_{x0})\Phi_{,\alpha} \wedge \mathbf{e}_r] + 3(\mathbf{e}_r\Phi_{,\alpha})[(\mathbf{F}_{,\beta}, \mathbf{n}_{x0}, \mathbf{e}_r)\mathbf{e}_r + (\mathbf{n}_{x0}\mathbf{e}_r)\mathbf{e}_r \wedge \mathbf{F}_{,\beta}]\}. \tag{2}$$

In relation (2), ε_{ijk} is the Levi-Civita symbol. The function F is defined by $F: \Delta \ni (u_1, u_2) \to x$, α, $\beta \in \{1, 2\}$

For $\mathrm{Ker_{cr}}$: $(u_1, u_2) = (x_1, x_2)$, $F = F_{\mathrm{cr}}$, $\Phi = \Phi_{\mathrm{cr}}$, $\mathbf{n}_{x0} = \mathbf{e}_3$
For $\mathrm{Ker_{lat}}$: $(u_1, u_2) = (\theta, x_3)$, $F = F_{\mathrm{lat}}$, $\Phi = \Phi_{\mathrm{lat}}$, $\mathbf{n}_{x0}$ is the outward normal at the point x_0 to the lateral surface.

The symbol *pv* before $\int$ indicates that the integral is understood in the sense of the principal value.

Partial derivatives of any function f with respect to variables u_i is denoted $f_{,i}$. Implicit summation is made over any repeated index.

The stress vector at the point x_0 is written in (1) as the sum of the surface intergals over the crack and the lateral surface of the bar. Eventually one has to solve the coupled set of equations (1) with unknowns φ_{cr} and φ_{lat}.

3. Numerical results

For all numerical purposes, the Poisson's ratio ν is taken as equal to 0.3. Both the crack and the lateral surface are discretized into finite elements and Eqns. (1) are solved by the collection method. Figure 6 shows a typical mesh modelling the cracked bar. Eight-node or six-node isoparametric 2D elements are used throughout the structure. Quarter-point elements [25] are specifically used along the crack front. Depending on the surface to which the element belongs, the geometry transformation and the interpolation of the density are performed with different variables [26]:

- for elements belonging to the crack surface, the mapped variables through geometric transformation are Cartesian co-ordinates $(x_1, x_2) \in \Delta_{\mathrm{cr}}$ and the interpolated functions are Cartesian components of φ_{cr}, φ_1, φ_2 and φ_3
- for elements belonging to the lateral surface of the bar, the mapped variables are cylindrical coordinates $(\theta, x_3) \in \Delta_{\mathrm{lat}}$ and the interpolated functions are here again Cartesian components of φ_{lat} for simplicity. Cylindrical variables (θ, x_3) allow us to shape the finite elements into *curved* elements fitting the cylindrical surface. However, this cannot be seen in Fig. 6 since the sides of the elements are represented by segments.

The mesh covers the crack surface together with the lateral free surface. Of course, if the different loads were treated separately, then symmetries or skew-symmetries could be exploited in order to reduce the problem to the study of one quarter or one half of the bar, provided adequate boundary conditions are added. This approach is not chosen here for two reasons: first, the whole structure is preserved so that several loads can be applied simultaneously, thus requiring only one solution of the algebraic system. Secondly, the matrix of the system being fully populated and moreover non-symmetrical (as is the case with any boundary integral equation method), obtaining symmetrical or skew-symmetrical final results ensures the accuracy of input data.

Eventually, the solution of the discretized equation of (1) provides the densities φ_{cr} and φ_{lat}, which in turn yield the complete elastic solution for the problem of the cracked bar, in particular the stress intensity factors can be evaluated along the crack front. Figure 7 shows the deformation of the lateral surface under a tensile load and of the crack under torsion. The latter is strongly emphasized in order to make it visible, explaining why some points on the crack seem to overlap the crack surface.

The normalized stress intensity factors at any point located on the crack front are determined as follows, using the notations of Fig. 8:

(a) Case of a uniform pressure on the crack (tensile load):

$$\frac{K_I}{\sigma\sqrt{\pi a}} = \frac{1}{\sigma\sqrt{\pi a}}\frac{E}{8(1-\nu^2)}\lim_{\rho\to 0}\left\{\varphi_3\sqrt{\frac{2\pi}{\rho}}\right\} = \frac{2\pi\sqrt{2\pi}}{\sigma\sqrt{\pi a}}\lim_{\rho\to 0}\left\{\frac{E}{16\pi(1-\nu^2)}\frac{\varphi_3}{\sqrt{\rho}}\right\}, \tag{3.1}$$

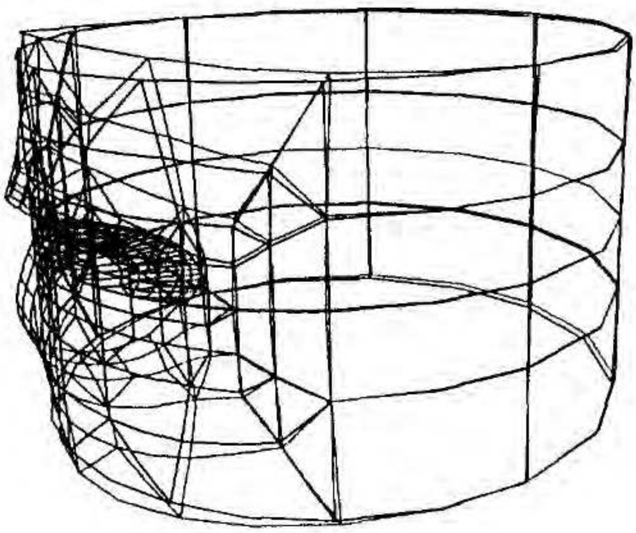

a

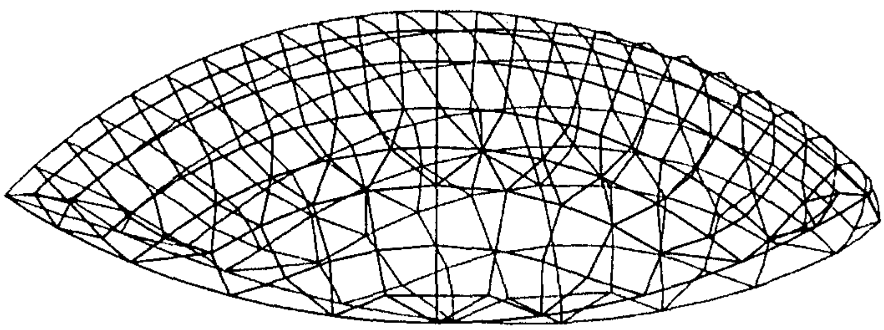

b

Fig. 7. (a) Deformation of the lateral surface under tensile loading. (b) Deformation of the crack under torsion.

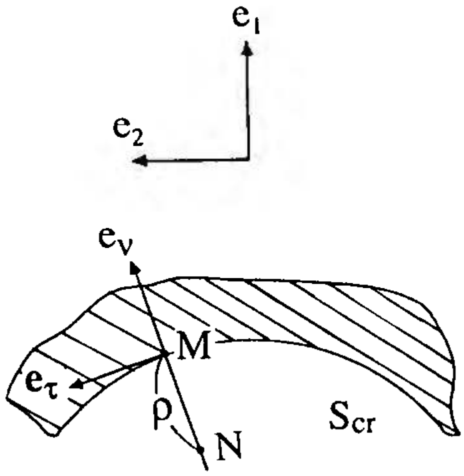

Fig. 8. Determination of stress intensity factors. ρ = Distance to the crack front. $\mathbf{e}_\nu$: in-plane normal to the crack front, outward with respect to the crack. $\mathbf{e}_\tau$: in-plane tangent, $\mathbf{e}_\tau = \mathbf{e}_3 \wedge \mathbf{e}_\nu$.

(b) case of a linear pressure on the crack (bending load):

$$\frac{K_{\mathrm{I}}}{\sigma_m\sqrt{\pi a}} = \frac{1}{\sigma_m\sqrt{\pi a}}\frac{E}{8(1-\nu^2)}\lim_{\rho\to 0}\left\{\varphi_3\sqrt{\frac{2\pi}{\rho}}\right\} = \frac{2\pi\sqrt{2\pi}}{\sigma_m\sqrt{\pi a}}\lim_{\rho\to 0}\left\{\frac{E}{16\pi(1-\nu^2)}\frac{\varphi_3}{\sqrt{\rho}}\right\}, \tag{3.2}$$

(c) case of a linear shear on the crack (torsion):

$$\frac{K_{\mathrm{II}}}{\tau_m\sqrt{\pi a}} = \frac{1}{\tau_m\sqrt{\pi a}}\frac{E}{8(1-\nu^2)}\lim_{\rho\to 0}\left\{\varphi_\nu\sqrt{\frac{2\pi}{\rho}}\right\} = \frac{2\pi\sqrt{2\pi}}{\tau_m\sqrt{\pi a}}\lim_{\rho\to 0}\left\{\frac{E}{16\pi(1-\nu^2)}\frac{\varphi_\nu}{\sqrt{\rho}}\right\}, \tag{3.3}$$

$$\frac{K_{\mathrm{III}}}{\tau_m\sqrt{\pi a}} = \frac{1}{\tau_m\sqrt{\pi a}}\frac{E}{8(1+\nu)}\lim_{\rho\to 0}\left\{\varphi_\tau\sqrt{\frac{2\pi}{\rho}}\right\} = \frac{2\pi\sqrt{2\pi}}{\tau_m\sqrt{\pi a}}(1-\nu)\lim_{\rho\to 0}\left\{\frac{E}{16\pi(1-\nu^2)}\frac{\varphi_\tau}{\sqrt{\rho}}\right\}, \tag{3.4}$$

where φ_ν, φ_τ, φ_3 are components of φ_{cr} in the local basis $(\mathbf{e}_\nu, \mathbf{e}_\tau, \mathbf{e}_3)$ generally varying along the crack front (Fig. 8).

It should be mentioned that relations (3) are taken just as *definitions* for series intensity factors *without* any assumption on the elastic state at the point of interest. Neither plane stress nor plane strain states, which are certainly predominant at the neighbourhood of the free surface or the deepest point of the crack, are assumed. The transition from one state to another will not be discussed in this paper.

As shown by (2), solving (1) gives directly $E/(16\pi(1-\nu^2))\varphi_{cr}$ – the term bracketed together in (3) – explaining why it is unnecessary to specify the value of Young's modulus E when computing stress intensity factors. Figure 9 shows the stress intensity factors obtained for the geometry corresponding to $a/R = 0.4$ and $\alpha = 1$, versus the relative abcissa s/s_m (Following the notations in Fig. 1, s is the curvilinear abcissa of a point on the crack front, s_m is arc length AB, $s/s_m = -1$ at B', $= +1$ at B).

Thus, for each geometry, 4 *discrete* curves are obtained corresponding respectively to K_{I} in tension, K_{I} in bending, K_{II} and K_{III} in twisting. As predicted, the K_{I} value in the bending case is always smaller than that in tensile loading at homologous points on the crack front. As for K_{III} values, they are found to be negative for all geometries. The negative sign of K_{III} is merely due to the fact that φ_3 equals the normal displacement at the upper crack face minus that at the lower face, and to the choice of the local basis orientation as shown in Fig. 8.

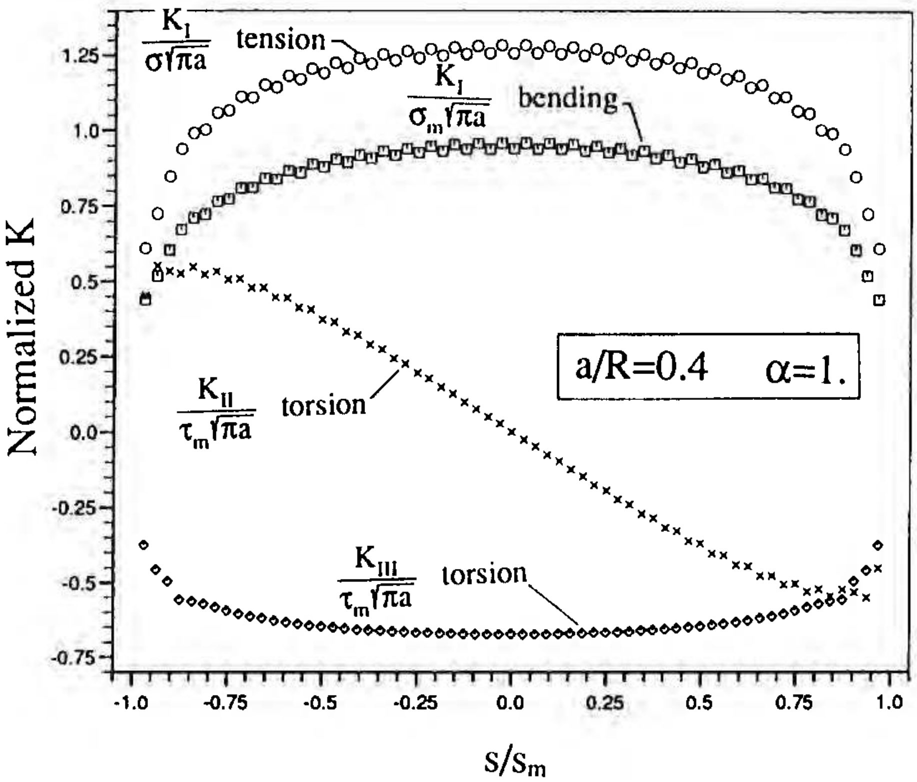

Fig. 9. Normalized stress intensity factors along the crack front. s = curvilinear abcissa, s_m = arc length AB (see Fig. 1).

Now using the least square method, the set of discrete values of stress intensity factors obtained for the 24 computed geometries are fitted in the following polynomial form:

(a) in the tension case: $$\frac{K_I}{\sigma\sqrt{\pi a}} = \sum_{i=0}^{3}\sum_{j=0}^{3}\sum_{k=0,2,4,6} C_{ijk}^{(It)}\left(\frac{a}{R}\right)^i \alpha^j \left(\frac{s}{s_m}\right)^k,$$

(b) in the bending case: $$\frac{K_I}{\sigma_m\sqrt{\pi a}} = \sum_{i=0}^{3}\sum_{j=0}^{3}\sum_{k=0,2,4,6} C_{ijk}^{(Ib)}\left(\frac{a}{R}\right)^i \alpha^j \left(\frac{s}{s_m}\right)^k, \tag{4}$$

(c) in the tension case: $$\frac{K_{II}}{\tau_m\sqrt{\pi a}} = \sum_{i=0}^{3}\sum_{j=0}^{3}\sum_{k=1,3} C_{ijk}^{(II)}\left(\frac{a}{R}\right)^i \alpha^j \left(\frac{s}{s_m}\right)^k,$$

$$\frac{K_{III}}{\tau_m\sqrt{\pi a}} = \sum_{i=0}^{3}\sum_{j=0}^{3}\sum_{k=0,2,4,6} C_{ijk}^{(III)}\left(\frac{a}{R}\right)^i \alpha^j \left(\frac{s}{s_m}\right)^k,$$

where the C_{ijk} coefficients are given in Table 2. All mean quadratic errors resulting from the fitting expressions (4) are about 1 percent, which is quite acceptable when compared to the accuracy of the finite element method. Expressions (4) should be used with crack depths of less than one-half diameter ($0 \leqslant a/R \leqslant 0.9$) and with $\alpha \in [0, 1]$. Figure 10 depicts the variation of normalized stress intensity factors K_I in tension and K_{II} in torsion as a function of the crack shape α and the relative abcissa s/s_m when the relative crack depth is 0.4. It is clearly shown that for nearly straight-fronted cracks ($\alpha \approx 1$) K_I is maximum at the deepest point of the crack ($s/s_m = 0$), and for semi-circular cracks ($\alpha \approx 0$) the maximum value for K_I is reached in the neighbourhood of the free surface ($|s/s_m| \approx 1$). As for K_{II}, it varies almost linearly with either α or s/s_m.

Table 2. C_{ijk} coefficients

i	j	k	$C_{ijk}^{(IT)}$ for tension	$C_{ijk}^{(Ib)}$ for bending	$C_{ijk}^{(III)}$ for torsion	i	j	k	$C_{ijk}^{(II)}$ for torsion
0	0	0	0.66837E+00	0.67003E+00	−0.48863E+00	0	0	1	−0.12653E+01
0	0	2	−0.12819E+00	−0.11851E+00	0.53272E+00	0	0	3	0.54361E+00
0	0	4	0.65362E+00	0.62139E+00	−0.66724E−01	0	1	1	0.28415E+01
0	0	6	−0.63476E+00	−0.60142E+00	−0.12661E+00	0	1	3	−0.89110E+00
0	1	0	0.14917E+01	0.14660E+01	−0.12523E+01	0	2	1	−0.29326E+01
0	1	2	−0.15181E+01	−0.14844E+01	−0.60349E+00	0	2	3	0.10159E+01
0	1	4	0.17418E+01	0.17943E+01	−0.49469E+01	0	3	1	0.11584E+01
0	1	6	−0.36700E+01	−0.36828E+01	0.70620E+01	0	3	3	−0.66930E+00
0	2	0	−0.17108E+01	−0.16117E+01	0.15275E+01	1	0	1	0.81442E+00
0	2	2	0.34585E+01	0.34011E+01	−0.16732E+00	1	0	3	−0.14275E+01
0	2	4	−0.11730E+02	−0.11906E+02	0.17182E+02	1	1	1	−0.13862E+02
0	2	6	0.14317E+02	0.14447E+02	−0.22195E+02	1	1	3	0.55863E+01
0	3	0	0.67685E+00	0.61063E+00	−0.66148E+00	1	2	1	0.12860E+02
0	3	2	−0.22663E+01	−0.22579E+01	0.53588E+00	1	2	3	−0.21359E+01
0	3	4	0.85036E+01	0.86794E+01	−0.11410E+02	1	3	1	−0.25711E+01
0	3	6	−0.93203E+01	−0.94854E+01	0.14460E+02	1	3	3	−0.10148E+00
1	0	0	0.27839E−01	−0.47133E+00	0.36699E+00	2	0	1	−0.15475E+01
1	0	2	0.17235E+01	0.20042E+01	−0.43199E+00	2	0	3	0.22907E+01
1	0	4	−0.62703E+01	−0.57214E+01	0.18574E+00	2	1	1	0.23260E+02
1	0	6	0.64590E+01	0.57645E+01	−0.19042E+00	2	1	3	−0.87984E+01
1	1	0	−0.81658E+01	−0.80954E+01	0.55393E+01	2	2	1	−0.15307E+02
1	1	2	0.17088E+02	0.16657E+02	−0.67371E+01	2	2	3	−0.76504E+01
1	1	4	−0.47996E+02	−0.46863E+02	0.48886E+02	2	3	1	−0.23390E+01
1	1	6	0.57275E+02	0.55311E+02	−0.56251E+02	2	3	3	0.10195E+02
1	2	0	0.18184E+02	0.16158E+02	−0.10060E+02	3	0	1	0.98730E+00
1	2	2	−0.51812E+02	−0.50220E+02	0.14305E+02	3	0	3	−0.16671E+01
1	2	4	0.18923E+03	0.18476E+03	−0.13617E+03	3	1	1	−0.13498E+02
1	2	6	−0.20458E+03	−0.19806E+03	0.16139E+03	3	1	3	0.35067E+01
1	3	0	−0.10094E+02	−0.85514E+01	0.49413E+01	3	2	1	0.53723E+01
1	3	2	0.34890E+02	0.33390E+02	−0.77503E+01	3	2	3	0.12547E+02
1	3	4	−0.13413E+03	−0.13068E+03	0.82669E+02	3	3	1	0.44763E+01
1	3	6	0.13902E+03	0.13465E+03	−0.99616E+02	3	3	3	−0.12247E+02
2	0	0	0.37008E+00	0.43077E+00	−0.16124E+00				
2	0	2	−0.48335E+01	−0.43163E+01	0.73697E−01				
2	0	4	0.18126E+02	0.15820E+02	0.44922E+00				
2	0	6	−0.18218E+02	−0.15788E+02	−0.11729E+00				
2	1	0	0.15716E+02	0.15715E+02	−0.98606E+01				
2	1	2	−0.33545E+02	−0.35751E+02	0.20672E+02				
2	1	4	0.94702E+02	0.10330E+03	−0.11358E+03				
2	1	6	−0.11449E+03	−0.11960E+03	0.11944E+03				
2	2	0	−0.40103E+02	−0.35295E+02	0.19091E+02				
2	2	2	0.11148E+03	0.11409E+03	−0.37027E+02				
2	2	4	−0.40124E+03	−0.41823E+03	0.27773E+03				
2	2	6	0.43253E+03	0.44272E+03	−0.30932E+03				
2	3	0	0.23819E+02	0.19974E+02	−0.98142E+01				
2	3	2	−0.77165E+02	−0.77778E+02	0.16355E+02				
2	3	4	0.29188E+03	0.30048E+03	−0.15546E+03				
2	3	6	−0.30135E+03	−0.30666E+03	0.17910E+03				
3	0	0	0.18566E+00	−0.80054E−01	0.55516E−01				
3	0	2	0.40254E+01	0.31925E+01	0.56762E−01				
3	0	4	−0.13204E+02	−0.11411E+02	−0.34231E+00				
3	0	6	0.13326E+02	0.11431E+02	0.97845E−01				
3	1	0	−0.76417E+01	−0.84732E+01	0.55027E+01				
3	1	2	0.16116E+02	0.19953E+02	−0.14710E+02				
3	1	4	−0.37988E+02	−0.53843E+02	0.74788E+02				

Table 2. contd.

i	j	k	$C_{ijk}^{(IT)}$ for tension	$C_{ijk}^{(Ib)}$ for bending	$C_{ijk}^{(III)}$ for torsion	i	j	k	$C_{ijk}^{(II)}$ for torsion
3	1	6	0.50833E+02	0.63937E+02	−0.74985E+02				
3	2	0	0.23886E+02	0.21101E+02	−0.10877E+02				
3	2	2	−0.59707E+02	−0.67447E+02	0.24614E+02				
3	2	4	0.20396E+03	0.24084E+03	−0.16937E+03				
3	2	6	−0.22429E+03	−0.25569E+03	0.18007E+03				
3	3	0	−0.13916E+02	−0.11863E+02	0.55202E+01				
3	3	2	0.42030E+02	0.46641E+02	−0.96793E+01				
3	3	4	−0.15616E+03	−0.17774E+03	0.88809E+02				
3	3	6	0.16211E+03	0.18102E+03	−0.98112E+02				

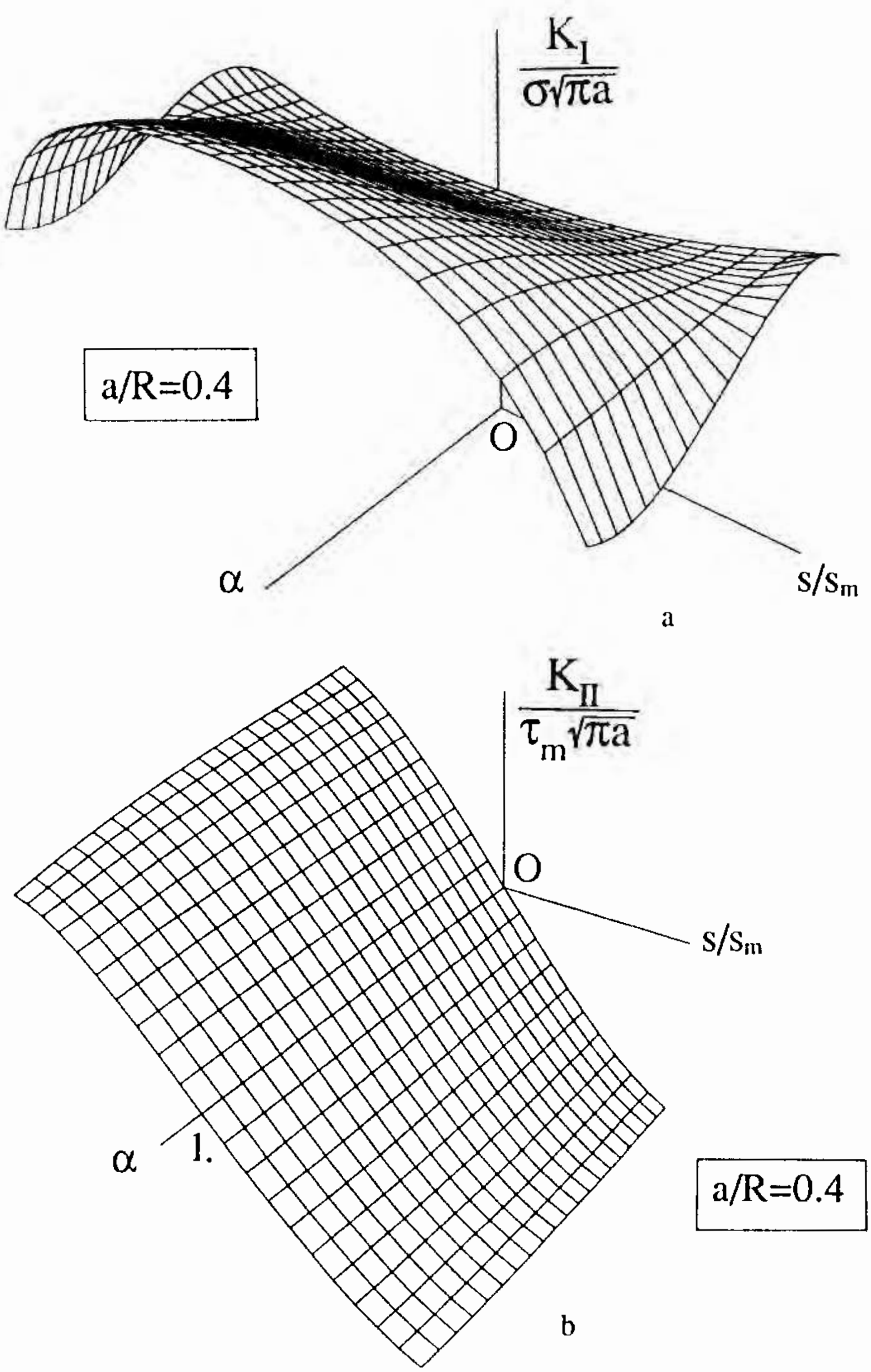

Fig. 10. Stress intensity factors as a function of the crack shape α and the relative abcissa s/s_m. (a) Normalized K_I in tension. (b) Normalized K_{II} in torsion.

3.1. *Stress intensity factors versus crack depth*

Here, consideration will be limited to the deepest point where the stress intensity factors are given from (4) by putting $s/s_m = 0$

$$\frac{K_A}{\sigma\sqrt{\pi a}} = \sum_i \sum_j C_{ij0}\left(\frac{a}{R}\right)^i \alpha^j, \tag{5}$$

where K stands for K_I, K_{II} or K_{III} and σ also stands for σ_m or τ_m. Figure 11 shows normalized K_I, K_{III} at the deepest point of the crack resulting from the basic loads – tension, bending and torsion – versus the relative crack depth a/R. Factor K_{II} is not plotted since it is identically zero at $s = 0$. For each load there are four K_I or K_{III} curves which relate individually to one crack shape, $\alpha = 0, \frac{1}{3}, \frac{2}{3}$ or 1. It can be seen that the stress intensity factors vary continuously with the crack shape but they are not necessarily monotone functions of the crack depth. For instance in Fig. 11a, the lower and upper curves related respectively to the semi-circular ($\alpha = 0$) and the straight-fronted crack ($\alpha = 1$) show that normalized K_{IA} increases with crack depth a, whereas the intermediate curves ($\alpha = \frac{1}{3}$ and $\alpha = \frac{2}{3}$) indicate that K_{IA}, which certainly increases with a,

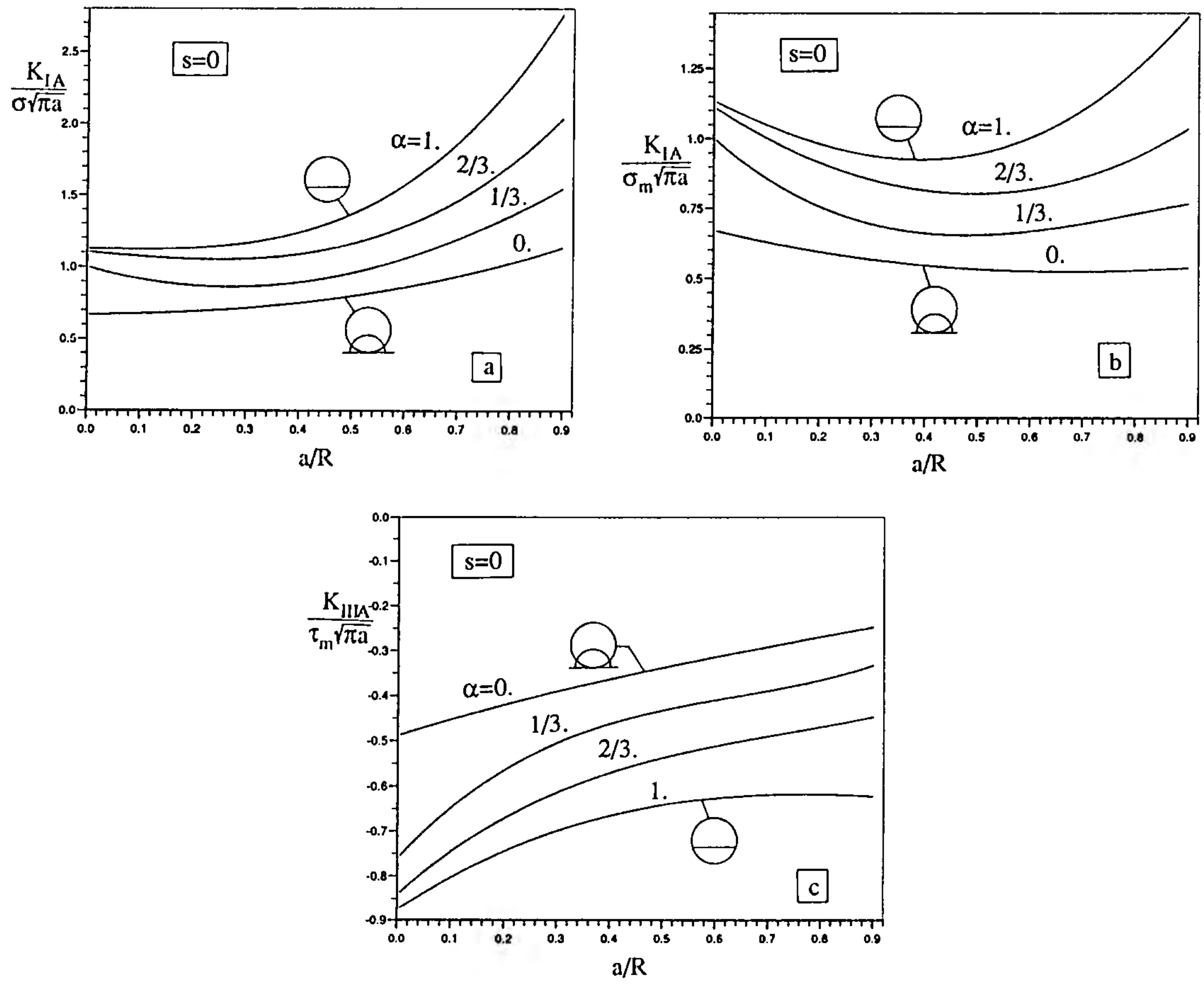

Fig. 11. Normalized stress intensity factors versus the relative crack depth. (a) Tension. (b) Bending. (c) Torsion.

decreases for small crack depths when normalized by $\sigma\sqrt{(\pi a)}$. It appears from Figs. 11a and b that when a/R takes the limit value zero, K_I at the deepest point takes almost the same value for the crack shapes $\alpha = 1$ and $\frac{2}{3}$. This would mean that, despite the notable change in radius of curvature – R' falling off from infinity when $\alpha = 1$ (straight-fronted crack) to a finite value when $\alpha = \frac{2}{3}$ – the stress intensity factors remain almost unchanged. In this respect, one can readily establish the limit value for radius R' when a/R tends to zero, the radius R of the bar and crack shape α being kept constant

$$\lim_{a/R \to 0} R' = \frac{\alpha^2}{1 - \alpha^2} R. \tag{6}$$

Relation (6) gives both trivial results – for $\alpha = 1$, R' tends to infinity and for $\alpha = 0$, R' tends to zero – and rather non-obvious results: for $\alpha = \frac{1}{3} R'$ tends to $R/8 = 0.125R$ and for $\alpha = \frac{2}{3} R'$ tends to $4R/5 = 0.8R$, as shown in Fig. 12.

3.2. Stress intensity factors along the crack front – Application to the crack growth behaviour problem

Figure 13 plots the normalized stress intensity factors versus relative abcissa s/s_m along the crack front, for the relative crack depth $a/R = 0.4$. Figure 13a shows more visibly than Fig. 10 that in the case of a tensile loading, the curvature of the K_I curve changes in sign when passing from the semi-circular crack ($\alpha = 0$) to the straight-fronted one ($\alpha = 1$). Meanwhile, in this instance when α is approximately $\frac{1}{3}$, a crack shape can be observed such that K_I remains virtually constant along the crack front. This means that if the iso-K_I criterion is chosen to predict the propagation of cracks created under mode I fatigue, the actual shape is that corresponding to $\alpha = \frac{1}{3}$.

Likewise, Fig. 13b shows that under a bending load the iso-K_I propagation criterion in this instance leads to the shape corresponding to $\alpha = \frac{2}{3}$.

More precisely, for a given crack depth, the crack shape satisfying the iso-K_I criterion can be computed in the following manner. Bearing in mind that R, α and σ are constant, deriving

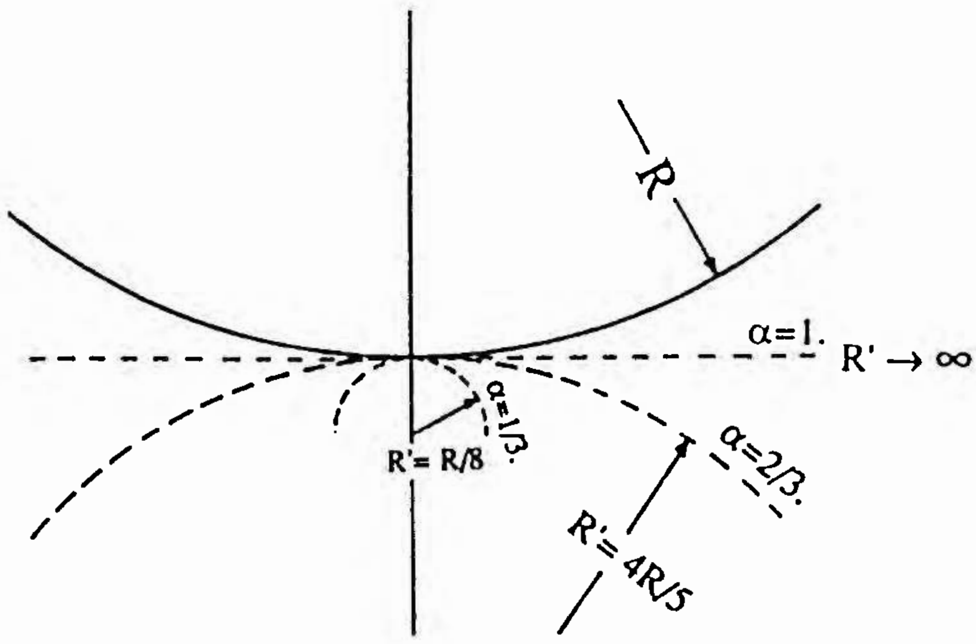

Fig. 12. Limit values of crack radius R' for very shallow surface cracks.

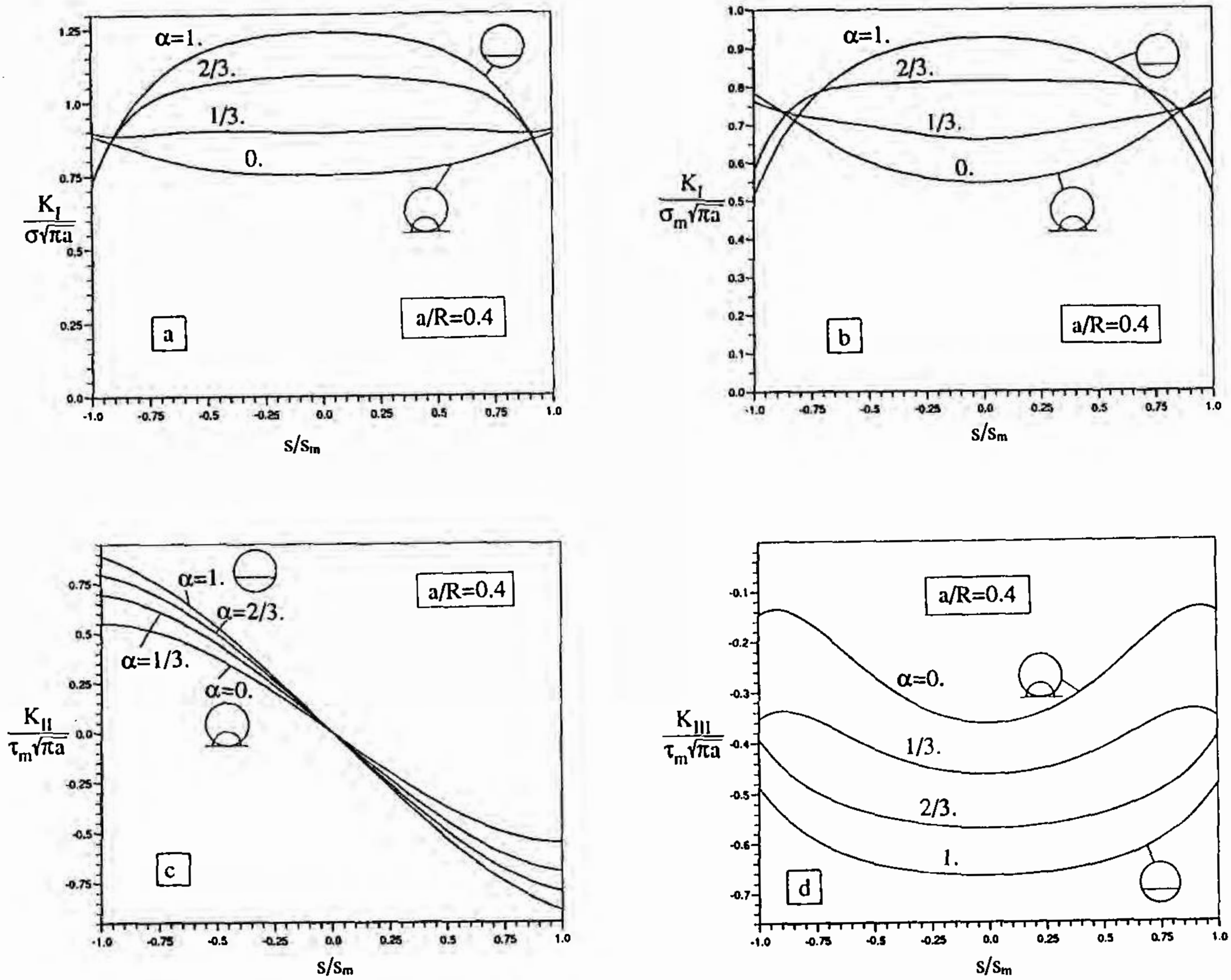

Fig. 13. Normalized stress intensity factors versus the relative abcissa on the crack front. (a) K_I in tension. (b) K_I in bending. (c) K_{II} in torsion. (d) K_{III} in torsion.

expression for K_I given in (4) with respect to the relative abcissa s/s_m yields

$$\frac{\partial K_I}{\partial\left(\dfrac{s}{s_m}\right)} = \sigma\sqrt{\pi a}\sum_i\sum_j\sum_{k\geqslant 1} kC_{ijk}\left(\frac{a}{R}\right)^i \alpha^j\left(\frac{s}{s_m}\right)^{k-1}. \tag{7}$$

As it is clear that the derivative of K_I cannot be identically equated to zero for all values of $s/s_m \in [-1, 1]$, the solution crack shape α is such that it minimizes max$\| \partial K_I/\partial(s/s_m) \|$, i.e. α is the solution of the min-max condition

$$\min_{\alpha\in[0,1]} \max_{s/s_m\in[-1,1]} \left\| \sum_i\sum_j\sum_{k\geqslant 1} kC_{ijk}\left(\frac{a}{R}\right)^i \alpha^j\left(\frac{s}{s_m}\right)^{k-1} \right\|. \tag{8}$$

In order to outline the crack propagation during mode I fatigue, (8) is approximately solved and the results obtained are within 5 percent accuracy. Table 3 lists the solution crack shapes α for the relative crack depths a/R considered in this paper.

Figure 14 compares the crack shapes predicted by the iso-K_I criterion with those of the cracks intersecting the free lateral surface at 90° angles. The latter cracks will be referred to, for brevity,

Table 3. Crack shapes verifying the iso-K_I criterion. Comparison with right angle cracks

	a/R	0.04	0.12	0.24	0.40	0.60	0.85
Iso-K_I criterion in TENSION	α	0.03	0.06	0.14	0.30	0.42	0.70
	R'/R	0.048	0.147	0.331	0.694	1.172	2.940
Iso-K_I criterion in BENDING	α	0.04	0.10	0.29	0.47	0.59	0.76
	R'/R	0.051	0.168	0.481	1.028	1.756	3.697
Right intersecting angle criterion	α	0.003	0.02	0.07	0.17	0.36	0.73
	R'/R	0.041	0.128	0.278	0.533	1.050	3.258

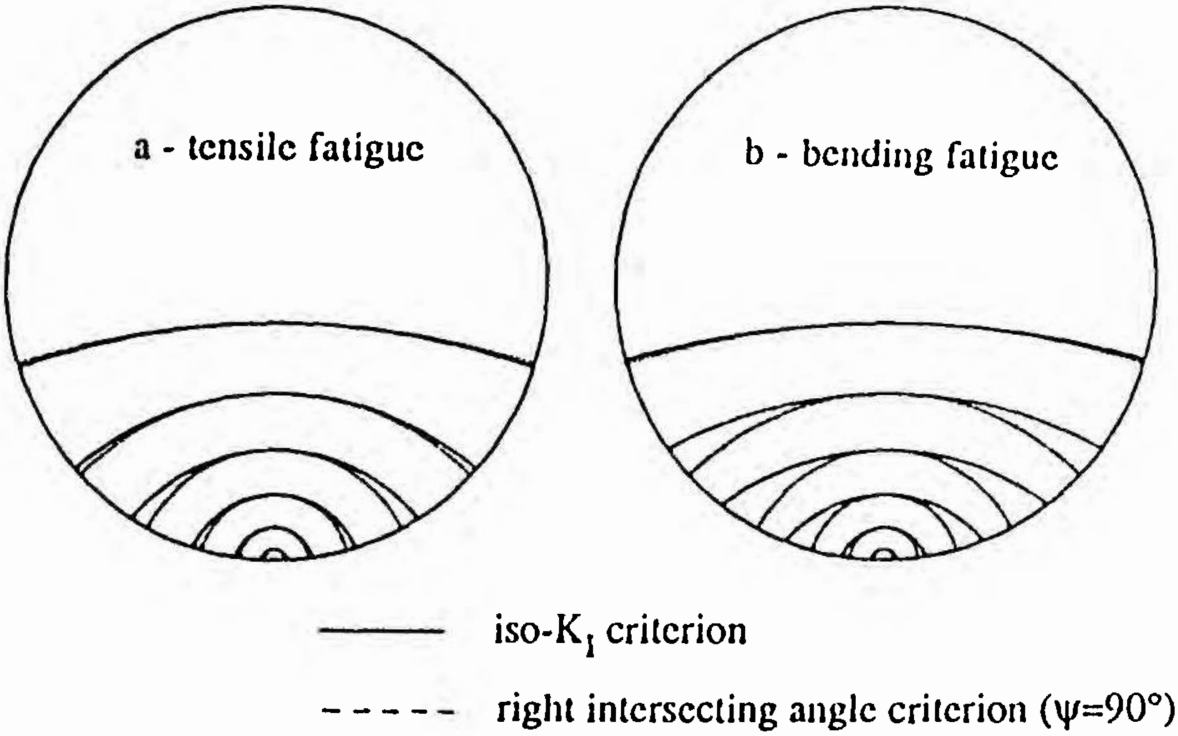

Fig. 14. Prediction of crack growth under mode I fatigue.

as 90° (intersecting) angle cracks. For such cracks, $\psi = 90°$ (Fig. 1) and one can readily prove that the crack radius R' is related to the radius R of the bar and the crack depth a by the relation

$$R' = \frac{a(2R - a)}{2(R - a)}. \tag{9}$$

It can be observed that the difference between iso-K_I cracks and 90° angle ones is fairly small in the case of tension (Fig. 14a) whereas this difference becomes notable for medium-sized cracks under bending (Fig. 14b). This would mean that in tensile load fatigue tests, cracks verifying the iso-K_I criterion are almost 90° angle cracks, while in bending fatigue tests this is true only for cracks with very small or very large depths. It should be remembered that this assessment has been made with ν equal to 0.3, and that the study of the influence of Poisson's ratio on the shape of cracks created by fatigue, which would not be negligible, is beyond the scope of this work.

Figures 15, 16 show the change in shape as the crack depth increases during the propagation. At the crack initiation, the crack is almost semi-circular. The further it grows up, i.e. the more the crack depth increases, the more it resembles a straight-fronted crack. Also represented in Figs. 15, 16 are the following stress intensity factors for a 90° angle crack: K_{I} at the deepest point 1 (in this case it is the minimum K_{I} on the crack front) and the average K_{I} denoted by $\bar{K}_{\mathrm{I}}$

$$\frac{\bar{K}_{\mathrm{I}}}{\sigma\sqrt{\pi a}} = \frac{1}{2s_m}\int_{-s_m}^{+s_m} \frac{K_{\mathrm{I}}}{\sigma\sqrt{\pi a}}\,\mathrm{d}s = \frac{1}{2}\int_{-1}^{+1} \frac{K_{\mathrm{I}}}{\sigma\sqrt{\pi a}}\,d\left(\frac{s}{s_m}\right) = \sum_i\sum_j\sum_k \frac{1}{k+1} C_{ijk}^{(\mathrm{I})}\left(\frac{a}{R}\right)^i \alpha^j. \tag{10}$$

It is clearly shown in Fig. 15 that for 90° angle cracks under tension, K_{IA} is approximately $\bar{K}_{\mathrm{I}}$ (the curves e and f are quite the same) and again one can recognize that 90° angle cracks verify the iso-K_{I} criterion. On the other hand, Fig. 16 shows that in the bending case, 90° angle cracks verify the iso-K_{I} criterion only for $a/R \approx 0$ and $a/R \approx 0.9$.

Figures 13c and 13d show the stress intensity factors K_{II} and K_{III} arising from a twisting moment applied at the ends of the bar. As already mentioned, K_{II} varies almost as a linear function of the curvilinear abcissa s. On the other hand, for all crack shapes the absolute value of K_{III} is maximal at the deepest point. In any case, the aspect of K_{II} and K_{III} curves are little influenced by the crack shape, contrary to what happens to K_{I}. Regarding the crack propagation behaviour with the presence of anti-plane shear, experimental investigations in pure mode III by [27] clearly show that the crack no longer grows by extending in its own plane but by

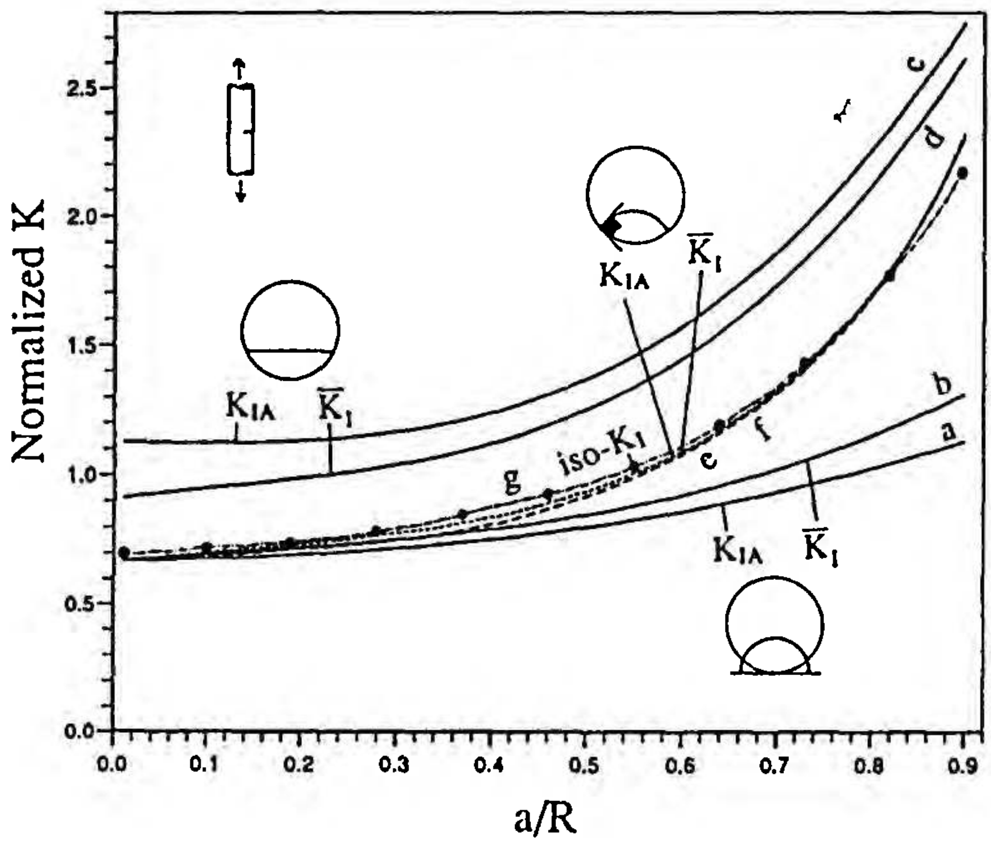

Fig. 15. Normalized K_{I} in tension at the deepest point and average normalized K_{I} for different crack shapes. Comparison with K_{I} computed from the iso-K_{I} criterion. (a) K_{I} at the deepest point for semi-circular cracks. (b) Average K_{I} for semi-circular cracks. (c) K_{I} at the deepest point for straight-fronted cracks. (d) Average K_{I} for straight-fronted cracks. (e) K_{I} at the deepest point for right angle cracks. (f) Average K_{I} for right angle cracks. (g) K_{I} for cracks verifying the iso-K_{I} criterion.

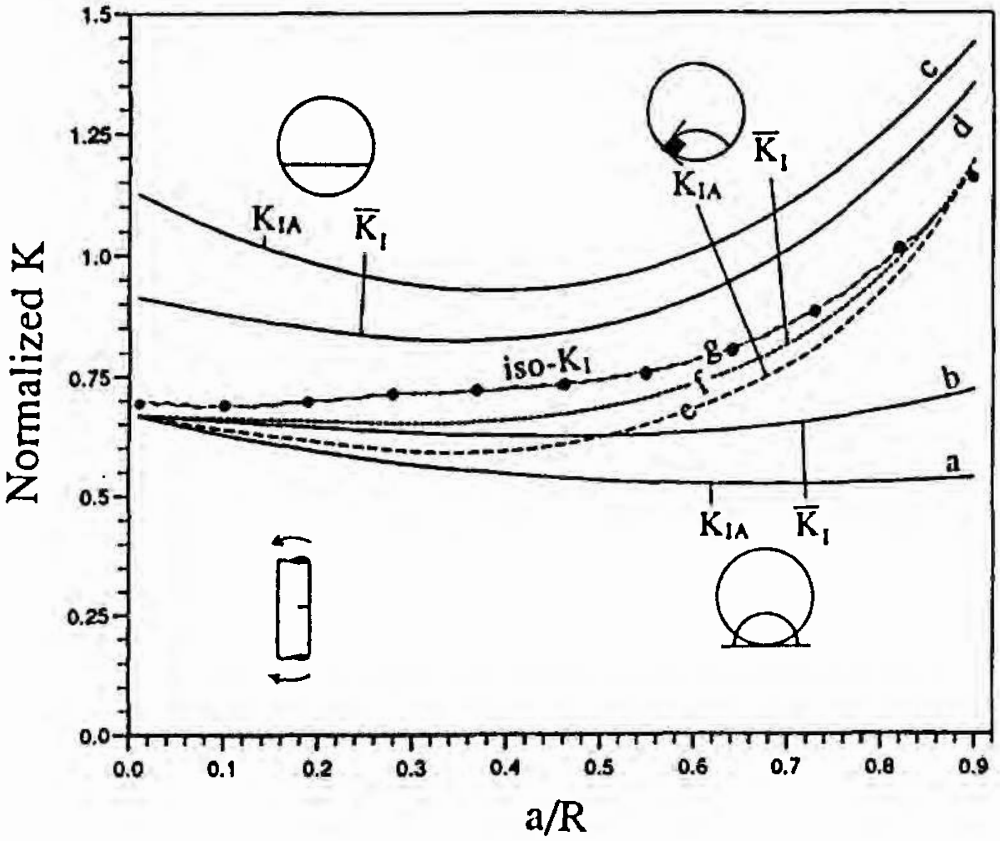

Fig. 16. Analogous to Fig. 15, the loading is now a bending.

generating multiple penny-shaped cracks which straddle the original crack front. The study of the crack deviation in a bar under torsion must be even more difficult at the points on the front, where K_{II} and K_{III} take comparable values. Similarly, under combined tensile and anti-plane shear loading (mode I + III), the crack grows by developing multiple lance-like fracture facets surrounding the crack front, as shown in [28]. These observations should be taken into account when the crack instability is studied under general loading conditions.

Lastly, it is noteworthy that the provided stress intensity factors values are valid only over about 80 percent of the crack front length. The K values for s/s_m approaching ± 1 are affected by phenomena extraneous to the present work, such as the vicinity of the surface terminal points B or B' (Fig. 1) that modifies the crack tip singularity. Also, the poor refinement of the finite element mesh around these zones must lower the accuracy of the numerical results. In any event, the results obtained in [29] prove that the crack tip singularity at the surface point depends on the Poisson ratio ν and the terminal point incident angle ψ (see Fig. 1) between the crack front and the surface line BB'. For a given value of ν, there exists a limiting value of ψ for which the stress intensity factor K_I tends to a non zero finite value. If ψ is less than this limit value, K_I falls off to zero and if ψ is greater, K_I becomes infinite. In both cases K_I classically defined loses its physical meaning.

4. Comparison with theoretical results

No theoretical results are available for surface cracks in round bars. However, stress intensity factors at the deepest point (point A in Fig. 1) of very shallow straight-fronted cracks can be effectively compared with analytical solutions for the single-edge crack in the half-space. This is due to the likeness between the latter geometry and the crack configuration viewed from point A when a/R tends to zero.

4.1. *Bar under tension*

The theoretical value for an edge crack of length a under a uniform pressure σ is given by Koiter [30]

$$K_{\mathrm{I}} = 1.1215\sigma\sqrt{(\pi a)}. \tag{11}$$

On the other hand, making a/R tend to zero in (5) gives

$$\lim_{a/R \to 0} \frac{K_{\mathrm{IA}}}{\sigma\sqrt{\pi a}} = \sum_j C_{0j0}^{(\mathrm{It})} \alpha^j, \tag{12}$$

which yields the limit value of normalized K_{I} at deepest point A of straight-fronted cracks

$$\lim_{a/R \to 0, \alpha = 1} \frac{K_{\mathrm{IA}}}{\sigma\sqrt{\pi a}} = \sum_j C_{0j0}^{(\mathrm{It})} = 1.126. \tag{13}$$

This value agrees well with the theoretical value (11) within an error of $+0.4$ percent. As regards the limit value of K_{IA} for semi-circular cracks when a/R tends to zero, one expects it to be greater than the theoretical value $2/\pi = 0.6366$ for the penny-shaped crack embedded in the infinite body, as is easily explained by the presence of the free lateral surface of the bar which must allow a wider crack opening, thus a greater K_{IA}. Indeed, here the limit value for semi-circular cracks is found to be 0.668, which is about 5 percent higher than the foregoing analytical value $2/\pi$.

Further, deriving expression (5) gives

$$\frac{\partial}{\partial(a/R)}\left(\frac{K_{\mathrm{IA}}}{\sigma\sqrt{\pi a}}\right) = \sum_{i \geqslant 1} \sum_j i C_{ij0}^{(\mathrm{It})} \left(\frac{a}{R}\right)^{i-1} \alpha^j. \tag{14}$$

Hence the slopes at $a/R = 0$ of the normalized K_{IA} curves are

$$\lim_{a/R \to 0, \alpha = 0} \frac{\partial}{\partial(a/R)}\left(\frac{K_{\mathrm{IA}}}{\sigma\sqrt{\pi a}}\right) = C_{100}^{(\mathrm{It})} = 0.028 = \tan^{-1} 2^\circ \tag{15}$$

$$\lim_{a/R \to 0, \alpha = 1} \frac{\partial}{\partial(a/R)}\left(\frac{K_{\mathrm{IA}}}{\sigma\sqrt{\pi a}}\right) = \sum_j C_{1j0}^{(\mathrm{It})} = -0.048 = \tan^{-1}(-3^\circ) \tag{16}$$

respectively for semi-circular and straight-fronted cracks. These are quite small values that compare well with the zero slope drawn from relation (11), $\lim \partial(K_{\mathrm{I}}/\sigma\sqrt{\pi a})/\partial(a/R) = 0$.

4.2. *Bar under bending*

From Table 2 one obtains the limit value of normalized K_I at deepest point A of straight-fronted cracks in the case of bending load

$$\lim_{a/R \to 0, \alpha = 1} \left(\frac{K_{IA}}{\sigma_m \sqrt{\pi a}} \right) = \sum_j C_{0j0}^{(Ib)} = 1.135. \tag{17}$$

This agrees well with Koiter's theoretical value [30] which is also valid in the bending case, within an error of $+1$ percent. Note that the slopes at $a/R = 0$ for semi-circular and straight-fronted cracks can also be computed in a similar way as in tensile loading

$$\lim_{a/R \to 0, \alpha = 0} \frac{\partial}{\partial(a/R)} \left(\frac{K_{IA}}{\sigma_m \sqrt{\pi a}} \right) = C_{100}^{(Ib)} = -0.471 = \tan^{-1}(-25^\circ), \tag{18}$$

$$\lim_{a/R \to 0, \alpha = 1} \frac{\partial}{\partial(a/R)} \left(\frac{K_{IA}}{\sigma_m \sqrt{\pi a}} \right) = \sum_j C_{1j0}^{(Ib)} = -0.961 = \tan^{-1}(-44^\circ), \tag{19}$$

although no easy comparison with theoretical values is possible to our knowledge.

4.3. *Bar under torsion*

Lastly, consider an edge crack of length a in the semi-infinite space, subjected to a uniform shear τ parallel to the crack front. The analytical result for the problem is given in [31]

$$K_{III} = -\tau\sqrt{(\pi a)}. \tag{20}$$

Applying the same reasoning to (5) as in proving (13), one obtains

$$\lim_{a/R \to 0, \alpha = 1} \frac{K_{IIIA}}{\tau_m \sqrt{\pi a}} = \sum_j C_{0j0}^{(III)} = -0.875. \tag{21}$$

This value is 13 percent higher than the theoretical value -1. The difference can be accounted for by the fact that the shear is in-plane stress. In Fig. 17, the hatched area represents the

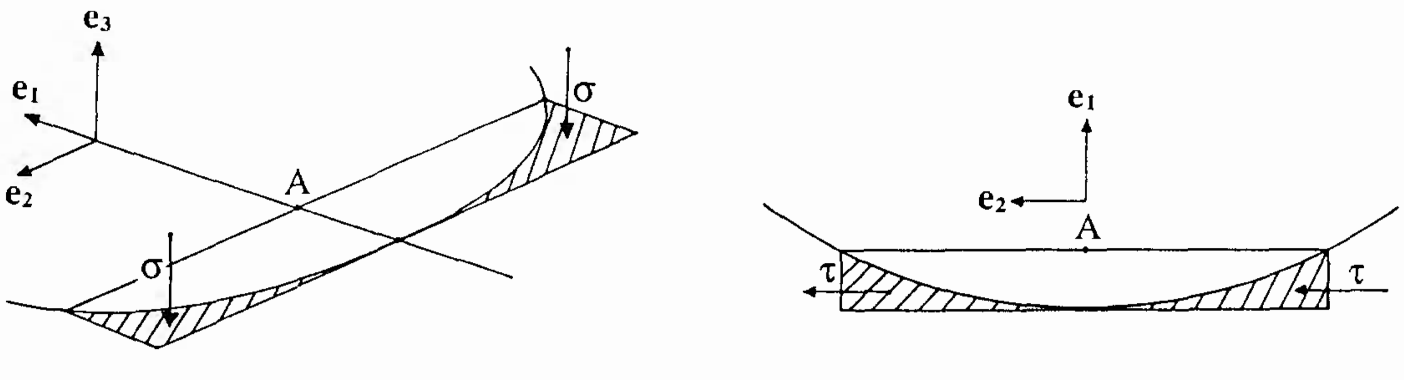

a b

Fig. 17. Difference between the problem of a crack in a round bar and that of an edge crack in the semi-infinite body.

difference between the problem of a shallow crack in a round bar and that of an edge crack in the semi-infinite medium. In mode I problems, the applied stresses are normal to this area and their effect can be neglected around the deepest point A of interest. On the contrary, in mode III problems the stresses are parallel to the crack front, hence they may have some influence on K_{III} at point A though applied on an area geographically remote.

5. Comparison with experimental results

Available results in the literature are mainly concerned with mode I and points A, B on the crack front (Fig. 1). Sometimes, K_I is even assumed to be constant on the crack front so that only the average value is considered. Therefore, the comparison with either experimental or numerical results can be made only in the tension and bending cases. Also, as discussed above, stress intensity factor values at the surface terminal point B will be discarded and only the values at the deepest point A – or the average values whenever they are given – are compared. We shall denote the diameter of the bar by D, $D = 2R$.

5.1. Bar under tension

Figure 18 compares K_I value of the present work with other authors' experimental values which are summarized below.

- *Straight-fronted cracks*

By the compliance method Daoud et al. [7] give the average normalized $\bar{K}_I$ for straight-fronted crack

$$\frac{\bar{K}_I}{\sigma\sqrt{\pi a}} = \frac{\sqrt{\pi}}{4\left(1 - \dfrac{a}{D}\right)^{1/4}} \sqrt{8.61 - 52.47\frac{a}{D} + 167.1\left(\frac{a}{D}\right)^2}, \quad 0.1 \leqslant a/D \leqslant 0.5. \tag{22}$$

Table 4 gives the normalized K_I at the deepest point A by photoelasticity determined by Astiz et al. [8]. In fact, the value 1.85 corresponding to $a/D = 0.45$ in this table will not be retained here as it is unreliable according to [8].

Bush [9] gives the compliance expression c in terms of the relative crack depth a/D

$$c = 0.0598723 + 0.2680344\left(\frac{a}{D}\right)^{2.8} + 0.2508381\left(\frac{a}{D}\right)^3 + 39.43071\left(\frac{a}{D}\right)^{12}, \tag{23}$$

which provides the average normalized $\bar{K}_I$ via the following relation

$$\frac{\bar{K}_I}{\sigma\sqrt{\pi a}} = \frac{\sqrt{\pi}}{4\sqrt{\dfrac{a}{D}}}\left(\frac{E}{1-\nu^2}\,\frac{D}{4}\,\frac{1}{[a/D - (a/D)^2]^{0.5}}\,\frac{dc}{d(a/D)}\right)^{0.5}. \tag{24}$$

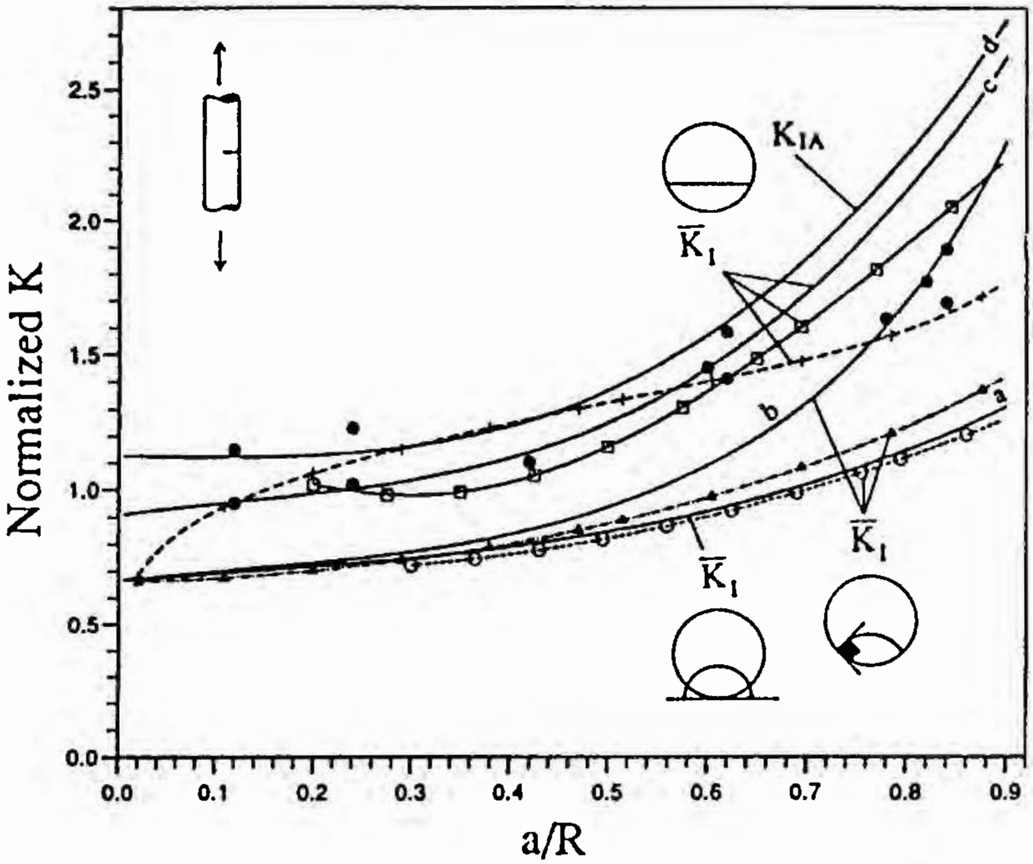

Fig. 18. Comparison with experimental results for K_I in tension: —□— : Daoud et al. [7]. ● : Astiz et al. [8]. — + — + Bush [9]. —○—○—: Wilhem et al. [4]. —▲— : Forman et al. [5], [32]. —— : Present results (a) Average K_I for semi-circular cracks. (b) Average K_I for right angle cracks. (c) Average K_I for straight-fronted cracks. (d) K_I at the deepest point for straight-fronted cracks.

The unity for compliance c in (23) is 10^{-6} in/lbf, Young's modulus in (24) is 10.6×10^6 psi, and $D = 3$ in. Attention should be drawn to the fact that in [9] the Poisson ratio is 0.32 and not 0.3 as assumed throughout this paper. However, the results are expected to be close enough to be comparable.

- *Cracks intersecting the lateral surface at right angles* ($\psi = 90°$, Fig. 1)

A special fatigue marking technique to outline the crack propagating allowed Wilhem et al. [4] to express the normalized K_I for right angle cracks, constant along the crack front, as

$$\frac{\bar{K}_I}{\sigma\sqrt{\pi a}} = 0.690 - 0.197\frac{a}{D} + 2.394\left(\frac{a}{D}\right)^2 + 1.965\left(\frac{a}{D}\right)^3, \quad 0.15 < a/D < 0.45. \tag{25}$$

Experiments conducted on fatigue cracks led Forman et al. [5], [32] to approximate the same quantity as

$$\frac{\bar{K}_I}{\sigma\sqrt{\pi a}} = 0.92\frac{2}{\pi}\sqrt{\frac{\tan\dfrac{\pi a}{2D}}{\dfrac{\pi a}{2D}}}\,\frac{1}{\cos\dfrac{\pi a}{2D}}\left[0.752 + 2.02\frac{a}{D} + 0.37\left(1 - \sin\frac{\pi a}{2D}\right)^3\right]. \tag{26}$$

(26) is reported as having good accuracy for $a/D \ll 1$, reasonable accuracy for $a/D < \frac{1}{2}$.

Table 4. Normalized K_I at the deepest point of straight-fronted cracks [8]

a/D	0.45	0.21	0.30	0.39	0.41	0.46		0.06	0.12	0.31	0.42
$K_{IA}/\sigma\sqrt{(\pi a)}$	1.85	1.10	1.45	1.63	1.77	1.91	1st series	1.15	1.02	1.58	1.89
							2nd series	0.95	1.23	1.41	1.69

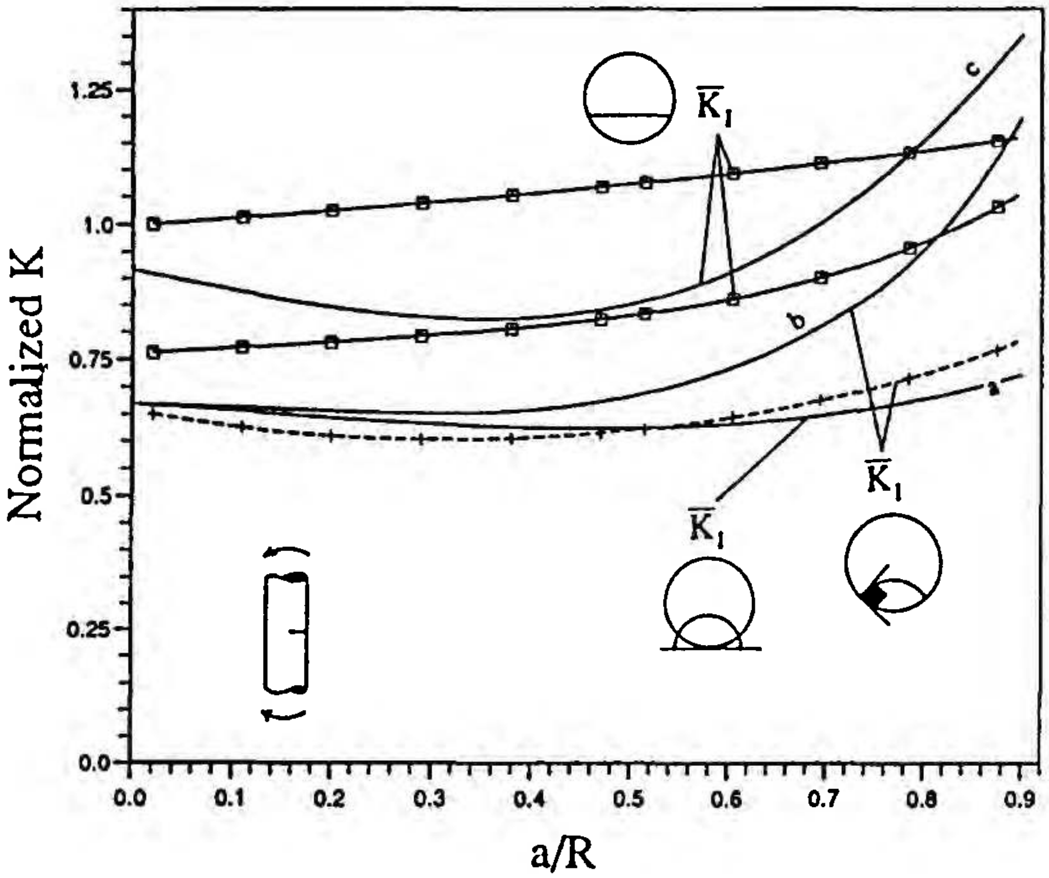

Fig. 19. Comparison with experimental results for K_I in bending: —□— : Bush [6]. — + — + — : Forman et al. [5]. ——— : Present results (a) Average K_I for semi-circular cracks. (b) Average K_I for right angle cracks. (c) Average K_I for straight-fronted cracks.

Figure 18 shows a good agreement between different results for small crack depths. Regarding large crack depths, other workers' results relating to 90° angle cracks are rather closer to present K_I for semi-circular cracks. As for straight-fronted cracks, the discrepancy becomes notable for large crack depths too.

5.2. *Bar under bending*

- *Straight-fronted cracks*

By means of compliance measurements Bush [6] provides the following equation for calculating the average stress intensity factor in the case of bending load

$$\frac{\bar{K}_I}{\sigma_m\sqrt{\pi a}} = \frac{\sqrt{\pi}}{32\sqrt{\dfrac{a}{D}}}\left(\frac{E}{1-\nu^2}\,\frac{D^3}{l^2}\,\frac{1}{[a/D-(a/D)^2]^{0.5}}\,\frac{dc}{d(a/D)}\right)^{0.5}, \tag{27}$$

where the compliance c is determined by either expression

$$c = 4.338749 + 23.66921\left(\frac{a}{D}\right)^{2.5} + 131.0767\left(\frac{a}{D}\right)^{7} \quad (10^{-6}\ \text{in/lbf}), \tag{28}$$

$$c = 0.2910587 + 2.54535\left(\frac{a}{D}\right)^{2.5} \quad (10^{-6}\ \text{in/lbf}). \tag{29}$$

Here again, $E = 10.6 \times 10^6$ psi. and $\nu = 0.32$. Relation (28) is used with diameter $D = 3$ in, relation (29) with $D = 6$ in. In both relations, length l is about 10 in.

- *Cracks intersecting the lateral surface at right angles*

Experiments conducted on fatigue cracks led Forman et al. [5] to the following approximate expression for the normalized K_I constant along the crack front

$$\frac{\bar{K}_I}{\sigma_m\sqrt{\pi a}} = 0.92\frac{2}{\pi}\sqrt{\frac{\tan\frac{\pi a}{2D}}{\frac{\pi a}{2D}}}\,\frac{1}{\cos\frac{\pi a}{2D}}\left[0.923 + 0.199\left(1 - \sin\frac{\pi a}{2D}\right)^4\right], \tag{30}$$

with the same accuracy reported above for the bar under tension.

- The comparison with all the available results for the bar under bending are shown in Fig. 19. For 90° angle cracks, a good agreement is observed at small crack depths only. As the crack depth increases, the experimental curve is rather closer to ours computed for semi-circular cracks. This remark agrees with Caspers et al.'s [19] following which 'the theory of perpendicular angles between crack front and shaft circumference seems to be approximately correct for pure bending up to an a/R-ratio of 1.0, but does not seem to be so applicable for tension, especially for increasing a/R-ratios'.

Concerning the straight-fronted cracks, the computed curve is within the range of Bush's experimental ones. Lastly, it should be mentioned that straight-fronted cracks do not exist naturally and they are actually very difficult to obtain in experimental works. In most cases, a sharp notch was machined to simulate the crack [6–9]. As the machined notch must be wider for a larger notch depth, it is unlikely to be comparable with a real crack. This should explain why the results agree less for large crack depths.

6. Comparison with numerical results

Here again, the comparisons are made in tension and bending cases. Moreover, only the K_I at the deepest point or its mean value is reported.

6.1. Bar under tension

Figure 20 shows all the numerical results for the case of a tensile load. Astiz [18] considered semi-elliptic cracks with axes a, b. The normalized K_I factor at the deepest point A is given as a

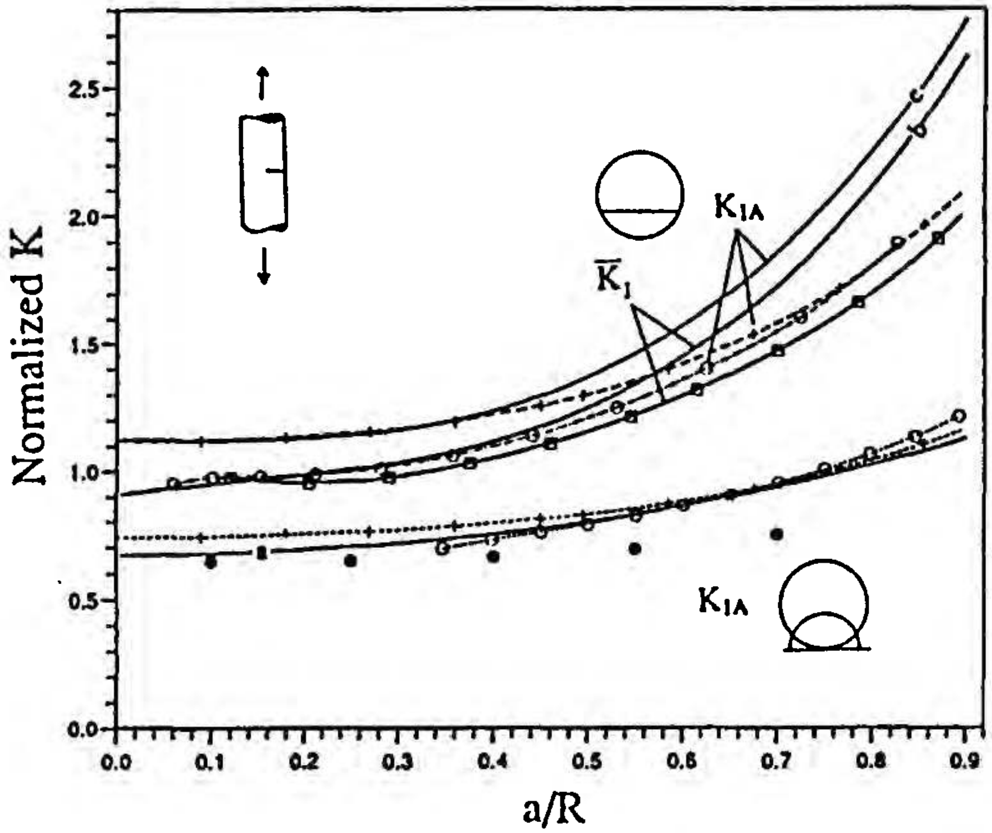

Fig. 20. Comparison with other numerical results for K_I in tension: —⊟— : Daoud et al. [7]. ● : Raju et al. [16]. $- + - +$: Astiz [18]. —⊖— : Caspers et al. [19]. ——— : Present results (a) K_I at the deepest point for semi-circular cracks. (b) Average K_I for straight-fronted cracks. (c) K_I at the deepest point for straight-fronted cracks.

polynomial function of the crack depth a/D and the aspect ratio a/b

$$\frac{K_{IA}}{\sigma\sqrt{\pi a}} = \sum_{i=0, i\neq 1}^{4} \sum_{j=0}^{3} C_{ij}\left(\frac{a}{D}\right)^i\left(\frac{a}{b}\right)^j. \tag{31}$$

The configurations which are comparable with those considered in this paper correspond to $a/b = 1$ (semi-circular cracks) and $a/b = 0$ (straight-fronted cracks).

Investigating part-circular cracks, Caspers et al. [19] also gives normalized K_I at the deepest point in the polynomial form

$$\frac{K_{IA}}{\sigma\sqrt{\pi a}} = \sum_{i=0}^{4} \sum_{j=1}^{5} C_{ij}^{(t)}\left(\frac{a_z}{R}\right)^i\left(\frac{\theta}{\pi}\right)^j, \tag{32}$$

where $a_z = a - R(1 - \cos\theta)$, θ is the angle at the centre sustended by the arc BB' (Fig. 1).

Raju et al. [16] considered nearly semi-elliptical cracks such that the crack front intersected the lateral surface of the bar at 90° angles. It should be noticed that the so-called crack length in

Table 5. Normalized stress intensity factor at the deepest point [16]

a/D		0.050	0.125	0.200	0.275	0.350
$\pi/2 \times K_{IA}/\sigma\sqrt{\pi a}$	tensile load	1.012	1.015	1.038	1.087	1.175
	bending load	0.938	0.836	0.749	0.683	0.629

this reference is defined as the arc length measured along the cylindrical surface and not as the major axis of the (nearly) elliptic crack. Thus the results of this reference for $a/c = 1$ must be compared to others keeping in mind the difference between the analyzed geometries. The normalized stress intensity factor at point A for $a/c = 1$ are listed in Table 5.

- *Straight-fronted cracks*

Daoud et al. [7] computed K_{I} assumed to be constant along the crack front

$$\frac{\bar{K}_{\mathrm{I}}}{\sigma\sqrt{\pi a}} = 1.11 - 3.59\frac{a}{D} + 24.87\left(\frac{a}{D}\right)^2 - 53.39\left(\frac{a}{D}\right)^3 + 57.23\left(\frac{a}{D}\right)^4, \quad 0.06 \leqslant a/D \leqslant 0.7. \tag{33}$$

6.2. *Bar under bending*

Figure 21 shows all the numerical results for the case of a bending load. The normalized K_{I} at point A for $a/c = 1$ from Raju et al.'s work [16] is given in Table 5.

Considering a lateral bending load, Caspers et al. [19] express K_{I} at the deepest point in the same polynomial form as for tension load

$$\frac{K_{\mathrm{IA}}}{\sigma_m\sqrt{\pi a}} = \sum_{i=0}^{4}\sum_{j=1}^{5} C_{ij}^{(b)}\left(\frac{a_z}{R}\right)^i\left(\frac{\theta}{\pi}\right)^j. \tag{34}$$

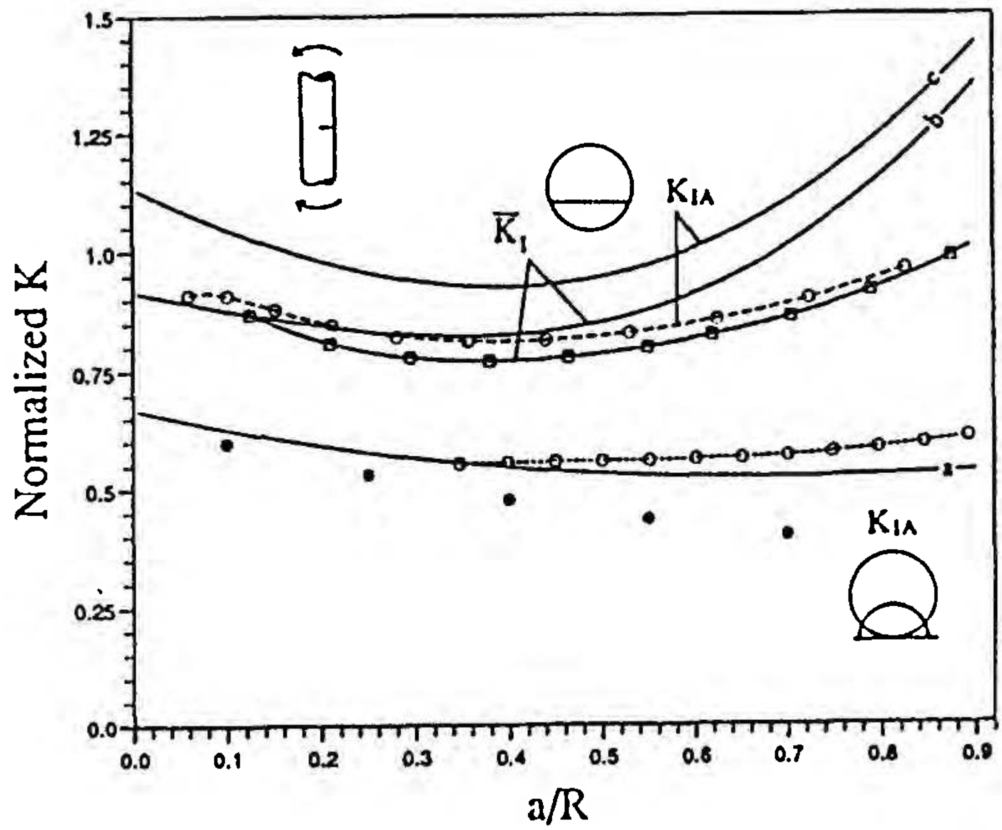

Fig. 21. Comparison with other numerical results for K_{I} in bending: □ : Daoud et al. [14]. ● : Raju et al. [16]. ○ : Caspers et al. [19]. —— : Present results (a) K_{I} at the deepest point for semi-circular cracks. (b) Average K_{I} for straight-fronted cracks. (c) K_{I} at the deepest point for straight-fronted cracks.

Table 6. Normalized K_I at the deepest point for a semi-circular crack in the half-space under tensile load. In parentheses: value given in the bending case.
Percent difference = (present result/referenced result − 1) × 100

Reference	Smith et al. (1967) [33]	Newman (1973) [34]	Nisitani et al. (1974) [35]	Newman et al. (1981) [36]	Isida et al. (1984) [37]	Present result
$K_{IA}/\sigma\sqrt{(\pi a)}$	0.656	0.656	0.636	0.662 (0.662)	0.659 (0.659)	0.668 (0.670)
Difference (percent)	2	2	5	1	1.4	

It should be mentioned that in [19] the linearly distributed stress is zero at the deepest point level ($x_1 = -R + a$, Fig. 1) and not at the diameter level ($x_1 = 0$). An adequate combination of (32) and (34) must be carried out to obtain the results for the bending case.

• *Straight-fronted cracks*
Daoud et al. [14] computed the average $\bar{K}_I$ over the crack front

$$\frac{\bar{K}_I}{\sigma_m\sqrt{\pi a}} = 1.04 - 3.64\frac{a}{D} + 16.86\left(\frac{a}{D}\right)^2 - 32.59\left(\frac{a}{D}\right)^3 + 28.41\left(\frac{a}{D}\right)^4,$$

$$0.0625 \leqslant a/D \leqslant 0.625. \tag{35}$$

• Figures 20 and 21 show a good agreement between different numerical results concerning semi-circular cracks, both in tension and bending cases. As regards straight-fronted cracks, the results agree well only for small crack depths. It should be mentioned that K_{IA} values for straight-fronted cracks given in [19] are rather low and thus are closer to $\bar{K}_I$.

• *Limiting configuration of very small semi-circular cracks*
Let us now consider the limiting case when the radius of the semi-circular crack $R' = a$ tends to zero. The limit value of K_I at the deepest point A is found to be 0.668 and 0.670, respectively, for the tensile and bending load. On the other hand, since this value must be the same as for a semi-circular crack in the half-space, it can be compared to the limit values obtained by earlier investigators treating the half-space problem. Table 6 shows that the differences are really small, except for Nisitani et al.'s value which amounts to 5 percent above the present result.

7. Conclusion

The obtained results have brought additional information to the problem of the elastic cracked bar, especially in mode I. A methodical use of integral equations has proved efficient in that it allows the following possibilities:

- the computation of stress intensity factors at any point of the crack front (except for the surface terminating points),
- the simultaneous study of modes I, II and III,

- the polynomial fitting of numerical values providing the stress intensity factors as functions of three geometrical parameters: the crack depth a, the crack radius R' and the abscissa s measured on the crack front,
- the results applicable to three basic loads: tension, bending and torsion.

Limiting values of stress intensity factors when the crack depth tends to zero have been found to be in full agreement with the theoretical values for the half-space problem. Furthermore, the numerical values have been compared with both experimental and numerical results available in the literature, which are mainly concerned with the opening mode. A good agreement between the different results has been observed for small crack depths. Nevertheless, for large crack depths for factor K_I increases more rapidly than others. The discrepancy is the more important for straight-fronted cracks.

Since no comparison is possible in modes II and III, it is assumed that the computation which is validated in mode I, also gives acceptable results for other modes. In fact, tests conducted on problems having known analytical solutions have shown that the numerical accuracy is higher in mode I problems than in others.

The polynomial fitting of the results has allowed a rapid and accurate calculation of the stress intensity factors as a function of the crack configuration and the applied loads. Also, the knowledge of these factors all along the crack front has made it possible to investigate either elastic fracture criteria or the fatigue crack growth behaviour. As an application of the results, the crack shapes verifying the iso-K_I criterion have been computed in mode I fatigue problems.

Of course, the obtained results are not influenced by the Young modulus value but they do depend on Poisson's ratio ν as shown by the governing equations (1) and (2). The computation has been carried out with ν equal to 0.3.

The effect of Poisson's ratio upon the crack shape can be investigated as an extension of the present work. Besides, the proposed integral equation formulation can be applied without major modifications to the problem of thick-walled cylinders containing through- or part-through cracks.

References

1. A. Athanassiadis, J.M. Boissenot, P. Brevet, D. François and A. Raharinaivo, *International Journal of Fracture* 17, 6 (1981) 553–566.
2. A.S. Salah el din and J.M. Lovegrove, *International Journal of Fatigue* 3 (1981) 117–123.
3. K. Nezu, S. Machida and H. Nakamura, in *The 25th Japan Congress on Material Research*, Metallic Metals (1982) 87–92.
4. D. Wilhem, J. FitzGerald, J. Carter and D. Dittmer, in *Advances in Fracture Research – Fracture 81. Proceedings of the 5th International Conference on Fracture Research (ICF-5)*, D. François (ed.), Pergamon Press (1982) 11–21.
5. R.G. Forman and V. Skivakumar, in *Fracture Mechanics*, vol. 17, ASTM STP 905, 17th National Symposium on Fracture Mechanics, Albany, New York (1986) 59–74.
6. A.J. Bush, in *Proceedings of the Society for Experimental Stress Analysis* 33, 2 (1976) 249–257.
7. O.E.K. Daoud, D.J. Cartwright and M. Carney, *Journal of Strain Analysis* 13, 2 (1978) 83–89.
8. M. Astiz, M. Elices, J. Morton and A. Valiente, in *Proceedings of the Society for Experimental Stress Analysis, Spring Meeting*, Dearborn, Michigan (1981) 277–282.
9. A.J. Bush, *Journal of Testing and Evaluation* 9, 4, July (1981) 216–233.
10. M.A. Astiz, M. Elices and A. Valiente, *European Congress on Fracture (ECF-6)* (1986) 65–74.
11. W.S. Blackburn, *Engineering Fracture Mechanics* 8 (1976) 731–736.
12. M.A. Astiz and M. Elices, in *Proceedings of the Second International Conference on Numerical Methods in Fracture Mechanics*, Pineridge Press, Swansea (1980) 93–106.

13. Y-X. Fan, Y-T. Fan and D-J. Fan, *Engineering Fracture Mechanics* 16, 1 (1982) 55–67.
14. O.E.K. Daoud and D.J. Cartwright, *Engineering Fracture Mechanics* 19, 4 (1984) 701–707.
15. O.E.K. Daoud and D.J. Cartwright, *Journal of Strain Analysis* 20, 1 (1985) 53–58.
16. I.S. Raju and J.C. Newman, in *Fracture Mechanics*, vol. 17, ASTM STP 905, 17th National Symposium on Fracture Mechanics, Albany, New York (1986) 789–805.
17. K.J. Nord and T.J. Chung, *International Journal of Fracture* 30 (1986) 47–55.
18. M.A. Astiz, *International Journal of Fracture* 31 (1986) 105–124.
19. M. Caspers and C. Mattheck, *Fatigue and Fracture of Engineering Materials Structures* 9, 5 (1987) 329–341.
20. J.H. Underwood and R.L. Woodward, *Experimental Mechanics* 29, 2 (1989) 66–168.
21. E. Si, *Engineering Fracture Mechanics* 37, 4 (1990) 805–812.
22. A. Levan and J. Royer, *International Journal of Fracture* 31 (1986) 125–142.
23. H.D. Bui, *Journal of Mechanics and Physics of Solids* 25 (1977) 29–39.
24. V.D. Kupradze, T.G. Gegelia, M.O. Bashelishvili and T.V. Burchuladze, *Three-dimensional Problems of the Mathematical Theory of Elasticity and Thermoelasticity*, North Holland (1979).
25. R.S. Barsoum, *International Journal of Numerical Methods in Engineering* 10, 1 (1976) 25–37.
26. A. Levan and B. Peseux, *International Journal for Numerical Methods in Engineering* 26 (1988) 2383–2402.
27. W.G. Knauss, *International Journal of Fracture* 6, 2 (1970) 183–187.
28. E. Sommer, *Engineering Fracture Mechanics* 1, 3 (1969) 539–546.
29. Z.P. Bazant and L.F. Estenssoro, *International Journal of Solids and Structures* 15 (1979) 405–426.
30. W.T. Koiter, *Journal of Applied Mechanics* 23 (1965) 237.
31. H. Tada, P. Paris and G. Irwin, *The Stress Analysis of Cracks Handbook*, Del Research Corporation (1973).
32. R.G. Forman, V. Shivakumar, J.C. Newman, L. Williams and S. Piotrowski, Fatigue crack growth computer program, NASA/FLAGRO, Version June (1985).
33. F.W. Smith, A.S. Kobayashi and A.F. Emery, *Journal of Applied Mechanics*, December (1967) 953–959.
34. J.C. Newman, *Engineering Fracture Mechanics* 5 (1973) 667–689.
35. H. Nisitani and Y. Murakami, *International Journal of Fracture* 10, 3 (1974) 353–368.
36. J.C. Newman and I.S. Raju, *Engineering Fracture Mechanics* 15, 1–2 (1981) 185–192.
37. M. Isida, H. Noguchi and T. Yoshida, *International Journal of Fracture* 2 (1984) 157–188.